# On the Dimensionality of Deformable Face Models

**CMU-RI-TR-06-12**

**Iain Matthews, Jing Xiao, and Simon Baker**

The Robotics Institute
Carnegie Mellon University
5000 Forbes Avenue
Pittsburgh, PA 15213

## Abstract

Model-based face analysis is a general paradigm with applications that include face recognition, expression recognition, lipreading, head pose estimation, and gaze estimation. A face model is first constructed from a collection of training data, either 2D images or 3D range scans. The face model is then fit to the input image(s) and the model parameters used in whatever the application is. Most existing face models can be classified as either 2D (e.g. Active Appearance Models) or 3D (e.g. Morphable Models.) In this paper we compare 2D and 3D face models along four axes: (1) representational power, (2) construction, (3) real-time fitting, and (4) self occlusion reasoning. For each axis in turn, we outline the differences that result from using a 2D or a 3D face model.

**Keywords:** Model-based face analysis, 2D Active Appearance Models, 3D Morphable Models, representational power, model construction, non-rigid structure-from-motion, factorization, real-time fitting, the inverse compositional algorithm, constrained fitting, occlusion reasoning.

# 1 Introduction

Model-based face analysis is a general paradigm with numerous applications. A face model is first constructed from either a set of 2D training images [Cootes *et al.*, 2001] or a set of 3D range scans [Blanz and Vetter, 1999]. The face model is then fit to the input image(s) and the model parameters are used in whatever the application is. In [Lanitis *et al.*, 1997], the same face model was used for face recognition, pose estimation, and expression recognition. Other applications include lip-reading [Matthews *et al.*, 2002] and gaze estimation [Ishikawa *et al.*, 2004].

Perhaps the most well known face models are 2D Active Appearance Models (AAMs) [Cootes *et al.*, 2001] and 3D Morphable Models (3DMMs) [Blanz and Vetter, 1999]. More recently, [Xiao *et al.*, 2004a] introduced 2D+3D Active Appearance Models, a model with the real-time fitting of 2D AAMs and the 3D modeling of 3DMMs. 2D+3D AAMs are constructed from 2D images using a non-rigid structure-from-motion algorithm such as the linear algorithm in [Xiao *et al.*, 2004b].

AAMs and 3DMMs are similar in many ways. Both consist of a linear shape model and a linear appearance (texture) model. The main difference between them is that the shape component of an AAM is 2D, whereas the shape component of a 3DMM is 3D. A natural question, then, is "what are the relative advantages and disadvantages of 2D and 3D face models?" In this paper, we attempt to answer this question by comparing 2D and 3D face models along four different axes: (1) representational power, (2) construction, (3) real-time fitting, and (4) occlusion reasoning. With the exception of the background material in Section 2, our discussion is on the level of general 2D and 3D linear face models, rather than comparing specific models such as AAMs and 3DMMS.

In Section 3 we compare the representational power of 2D and 3D linear face models. We prove 3 main results. (1) Under the scaled orthographic image formation model, 2D and 3D face models have the same power to represent 3D objects; i.e. any shape model that can be generated by a 3D model can also be generated by a 2D model. (2) Up to 6 times as many parameters may be required by the 2D model to represent the same phenomenon as the 3D model. (3) In general, a 2D model can generate model instances that are not possible to generate with the corresponding 3D model; i.e. some (actually most) 2D model instances are "physically unrealizable."

In Section 4 we compare the construction of 2D and 3D models. We show how a non-rigid structure-from-motion algorithm can be used to construct a 3D face model from a 2D model (and 2D tracking results.) We also present an algorithm for the construction of a 2D model from a 3D model and show how it can be used to build 2D face models that better model rotated faces.

In Section 5 we study the real-time fitting of face models. We begin by reviewing the efficient "inverse compositional" 2D fitting algorithm [Matthews and Baker, 2004]. We then show that the naive 3D generalization of this algorithm violates one of the key assumptions made by the 2D algorithm. The 3D generalization is therefore not a correct algorithm. We describe a "work around" to this problem, the simultaneous fitting of both a 2D and a 3D shape model. We show how this formulation of the 3D fitting problem does lead to a real-time implementation. We empirically compare the 2D fitting algorithm with its 3D extension. The results show that fitting a 3D model is: (1) inherently more robust than fitting a 2D model, and (2) takes fewer iterations to converge.

In Section 6 we consider self occlusion reasoning. We describe the natural 3D "z-buffering" algorithm and a 2D approximation to it that assumes that the head is convex. We empirically compare the performance of these algorithms and show that in practice they perform similarly.

# 2 Background

We begin with a brief review of 2D Active Appearance Models (AAMs) [Cootes *et al.*, 2001] and 3D Morphable Models (3DMMs) [Blanz and Vetter, 1999]. We have taken the liberty to simplify the presentation and change the notation from [Cootes *et al.*, 2001] and [Blanz and Vetter, 1999] to highlight the similarities and differences between the two types of models. Note that our definition of an AAM corresponds to that of an "Independent AAM" in [Matthews and Baker, 2004].

## 2.1 2D Active Appearance Models

The *2D shape* of an Active Appearance Model (AAM) is defined by a 2D triangulated mesh and in particular the vertex locations of the mesh. Mathematically, the shape $\mathbf{s}$ of an AAM is defined

as the 2D coordinates of the $n$ vertices that make up the mesh:

$$\mathbf{s} = \begin{pmatrix} u_1 & u_2 & \dots & u_n \\ v_1 & v_2 & \dots & v_n \end{pmatrix}. \tag{1}$$

AAMs allow linear shape variation. This means that the shape matrix $\mathbf{s}$ can be expressed as a base shape $\mathbf{s}_0$ plus a linear combination of $m$ shape matrices $\mathbf{s}_i$:

$$\mathbf{s} = \mathbf{s}_0 + \sum_{i=1}^{m} p_i \, \mathbf{s}_i \tag{2}$$

where the coefficients $\mathbf{p} = (p_1, \dots, p_m)^{\mathrm{T}}$ are the shape parameters.

AAMs are normally computed from training data consisting of a set of images with the shape mesh (usually hand) marked on them [Cootes *et al.*, 2001]. The Iterative Procrustes Algorithm and Principal Component Analysis (PCA) are then applied to compute the base shape $\mathbf{s}_0$ and the shape variation $\mathbf{s}_i$. The base shape $\mathbf{s}_0$ is the mean shape computed by the Procrustes algorithm and the matrices $\mathbf{s}_i$ are the (reshaped) PCA eigenvectors corresponding to the $m$ largest eigenvalues.

The *appearance* of the AAM is defined within the base mesh $\mathbf{s}_0$. Let $\mathbf{s}_0$ also denote the set of pixels $\mathbf{u} = (u, v)^{\mathrm{T}}$ that lie inside the base mesh $\mathbf{s}_0$, a convenient notational shortcut. The appearance of the AAM is then an image $A(\mathbf{u})$ defined over the pixels $\mathbf{u} \in \mathbf{s}_0$. AAMs allow linear appearance variation. This means that the appearance $A(\mathbf{u})$ can be expressed as a base appearance $A_0(\mathbf{u})$ plus a linear combination of $l$ appearance images $A_i(\mathbf{u})$:

$$A(\mathbf{u}) = A_0(\mathbf{u}) + \sum_{i=1}^{l} \lambda_i \, A_i(\mathbf{u}) \tag{3}$$

where the coefficients $\boldsymbol{\lambda} = (\lambda_1, \dots, \lambda_l)^{\mathrm{T}}$ are the appearance parameters. The base appearance $A_0$ and appearance modes $A_i$ are usually computed by applying PCA to the shape normalized training images [Cootes *et al.*, 2001]. The base appearance $A_0$ is the mean appearance and the appearance images $A_i$ are the PCA eigenvectors corresponding to the $l$ largest eigenvalues.

Although Equations (2) and (3) describe the AAM shape and appearance variation, they do

not describe how to generate an AAM *model instance.* AAMs use a simple 2D image formation model (sometimes called a normalization), a 2D similarity transformation $\mathbf{N}(\mathbf{u};\mathbf{q})$, where $\mathbf{q} = (q_1, \ldots, q_4)^{\mathrm{T}}$ contains the rotation, translation, and scale parameters [Matthews and Baker, 2004]. Given the AAM shape parameters $\mathbf{p} = (p_1, \ldots, p_m)^{\mathrm{T}}$, Equation (2) is used to generate the shape of the AAM $\mathbf{s}$. The shape $\mathbf{s}$ is then mapped into the image with the similarity transformation to give $\mathbf{N}(\mathbf{s};\mathbf{q})$. Equation (3) is used to generate the AAM appearance $A(\mathbf{u})$ from the AAM appearance parameters $\boldsymbol{\lambda} = (\lambda_1, \ldots, \lambda_l)^{\mathrm{T}}$. The AAM model instance with shape parameters $\mathbf{p}$, image formation parameters $\mathbf{q}$, and appearance parameters $\boldsymbol{\lambda}$ is then created by warping the appearance $A(\mathbf{u})$ from the base mesh $\mathbf{s}_0$ to the model shape mesh in the image $\mathbf{N}(\mathbf{s};\mathbf{q})$. In particular, the pair of meshes $\mathbf{s}_0$ and $\mathbf{N}(\mathbf{s};\mathbf{q})$ define a piecewise affine warp from $\mathbf{s}_0$ to $\mathbf{N}(\mathbf{s};\mathbf{q})$ which we denote $\mathbf{N}(\mathbf{W}(\mathbf{u};\mathbf{p});\mathbf{q})$. For each triangle in $\mathbf{s}_0$ there is a corresponding triangle in $\mathbf{N}(\mathbf{s};\mathbf{q})$ and each pair of triangles defines a unique affine warp. See [Matthews and Baker, 2004] for more details.

## 2.2 3D Morphable Models

The *3D shape* of a 3D Morphable Model (3DMM) is defined by a 3D triangulated mesh. Mathematically, we define the shape $\overline{\mathbf{s}}$ of a 3DMM as the 3D coordinates:

$$\overline{\mathbf{s}} \;=\; \begin{pmatrix} x_1 & x_2 & \ldots & x_{\overline{n}} \\ y_1 & y_2 & \ldots & y_{\overline{n}} \\ z_1 & z_2 & \ldots & z_{\overline{n}} \end{pmatrix} \tag{4}$$

of the $\overline{n}$ vertices that make up the mesh. 3DMMs allow linear shape variation. The shape matrix $\overline{\mathbf{s}}$ can be expressed as a base shape $\overline{\mathbf{s}}_0$ plus a linear combination of $\overline{m}$ shape matrices $\overline{\mathbf{s}}_i$:

$$\overline{\mathbf{s}} \;=\; \overline{\mathbf{s}}_0 + \sum_{i=1}^{\overline{m}} \overline{p}_i\, \overline{\mathbf{s}}_i. \tag{5}$$

where the coefficients $\overline{\mathbf{p}} = (\overline{p}_1, \ldots, \overline{p}_{\overline{m}})^{\mathrm{T}}$ are the 3D shape parameters.

3DMMs are normally computed from training data consisting of a number of 3D *range* scans

with the mesh vertices located in them [Blanz and Vetter, 1999]. PCA is then applied to the 3D coordinates of the training meshes. The base shape $\overline{\mathbf{s}}_0$ is the mean shape and the matrices $\overline{\mathbf{s}}_i$ are the (reshaped) eigenvectors corresponding to the $\overline{m}$ largest eigenvalues.

The *appearance* of a 3DMM is defined within a 2D triangulated mesh that has the same topology (vertex connectivity) as the base 3D mesh $\overline{\mathbf{s}}_0$. Let $\overline{\mathbf{s}}_0^*$ denote the set of pixels $\mathbf{u} = (u, v)^{\mathrm{T}}$ that lie inside this 2D mesh. The appearance of the 3DMM is then an image $\overline{A}(\mathbf{u})$ defined over the pixels $\mathbf{u} \in \overline{\mathbf{s}}_0^*$. 3DMMs also allow linear appearance variation. The appearance $\overline{A}(\mathbf{u})$ can be expressed as a base appearance $\overline{A}_0(\mathbf{u})$ plus a linear combination of $\overline{l}$ appearance images $\overline{A}_i(\mathbf{u})$:

$$\overline{A}(\mathbf{u}) \;=\; \overline{A}_0(\mathbf{u}) + \sum_{i=1}^{\overline{l}} \overline{\lambda}_i \, \overline{A}_i(\mathbf{u}) \tag{6}$$

where the coefficients $\overline{\boldsymbol{\lambda}} = (\overline{\lambda}_1, \ldots, \overline{\lambda}_{\overline{l}})^{\mathrm{T}}$ are the appearance parameters. The base appearance $\overline{A}_0$ and the appearance images $\overline{A}_i$ are computed by applying PCA to the texture components of the range scans, appropriated warped onto the 2D triangulated mesh $\overline{\mathbf{s}}_0^*$ [Blanz and Vetter, 1999].

To generate a 3DMM *model instance* an image formation model is needed to convert the 3D shape $\overline{\mathbf{s}}$ into a 2D mesh, onto which the appearance is warped. As in [Romdhani and Vetter, 2003], we use the scaled orthographic model defined by the projection matrix:

$$\mathbf{P} \;=\; \begin{pmatrix} i_x & i_y & i_z \\ j_x & j_y & j_z \end{pmatrix} \tag{7}$$

and the offset of the origin $(o_u, o_v)^{\mathrm{T}}$. The two vectors $\mathbf{i} = (i_x, i_y, i_z)$ and $\mathbf{j} = (j_x, j_y, j_z)$ are the projection axes. We require that the projection axes are equal length and orthogonal; i.e. we require that $\mathbf{i} \cdot \mathbf{i} = i_x i_x + i_y i_y + i_z i_z = j_x j_x + j_y j_y + j_z j_z = \mathbf{j} \cdot \mathbf{j}$ and $\mathbf{i} \cdot \mathbf{j} = i_x j_x + i_y j_y + i_z j_z = 0$. The result of imaging the 3D point $\mathbf{x} = (x, y, z)^{\mathrm{T}}$ with this scaled orthographic model is the 2D point:

$$\mathbf{u} \;=\; \mathbf{P}\mathbf{x} + \begin{pmatrix} o_u \\ o_v \end{pmatrix}. \tag{8}$$

Note that the scaled orthographic projection has 6 degrees of freedom which can be mapped onto a 3D pose (yaw, pitch, roll), a 2D translation, and a scale. The 3DMM model instance is then computed as follows. Given the shape parameters $\overline{p}_i$, the 3D shape $\overline{\mathbf{s}}$ is computed using Equation (4). Each 3D vertex $(x_i, y_i, z_i)^{\mathrm{T}}$ is then mapped to a 2D vertex using Equation (8). (Note that during this process the visibility of the triangles in the mesh should be computed and respected. See Section 6 for more details.) The appearance is then computed using Equation (6) and warped onto the 2D mesh using the piecewise affine warp defined by the mapping from the 2D vertices in $\overline{\mathbf{s}}_0^*$ to the corresponding 2D vertices computed by the applying Equation (4) to the 3D shape $\overline{\mathbf{s}}$.

### 2.3 Similarities and Differences

AAMs and 3DMMs are similar in many ways. They both consist of a linear shape model and a linear appearance model. In particular, Equations (2) and (5) are almost identical. Equations (3) and (6) are also almost identical. The main difference between them is that the shape component of the AAM is 2D (see Equation (1)) whereas that of the 3DMM is 3D (see Equation (4)).

Note that there are other minor differences between 2D AAMs [Cootes *et al.*, 2001] and 3DMMs [Blanz and Vetter, 1999]. For example, (1) 3DMMs are usually constructed to be denser; i.e. consist of more triangles, and (2) because of their 3D shape and density, 3DMMs can also use the surface normal in their appearance model. In this paper, we address the differences between 2D and 3D face models in general, rather than specifically comparing AAMs and 3DMMS.

## 3 Representational Power

It is a common preconception that 3D models are "more powerful" than 2D models. In this section, we investigate to what extent this is really the case (for the scaled orthographic image formation model in Equation (8).) The shape of either a 2D or 3D model instance is a vector of 2D points in an image. In Section 3.1 we show that the set of all such 2D point vectors generated by a 3D model can also be generated by a 2D model. On the other hand, we also show that 3D models are more

compact than 2D models. In particular, we show that up to approximately 6 times as many shape parameters may be needed by a 2D model to represent the same phenomenon represented by a 3D model. Finally, in Section 3.2 we show that, in general, when a 2D model is used to model a 3D phenomenon the resulting 2D model can generate model instances that are not physically realizable (in the sense that there are valid 2D model instances that are not valid 3D model instances.) Note that the analysis in this section ignores occlusion which is covered in Section 6.

## 3.1 Equivalence and Number of Parameters

The shape variation of a 2D model is described by Equation (2) and $\mathbf{N}(\mathbf{u};\mathbf{q})$. That of an 3D model is described by Equations (5) and (8). We can ignore the offset of the origin $(o_u, o_v)^{\mathrm{T}}$ in the scaled orthographic model because this offset corresponds to a translation which can be modeled by the 2D similarity transformation $\mathbf{N}(\mathbf{u};\mathbf{q})$. The 2D shape variation of the 3D model is then:

$$\begin{pmatrix} i_x & i_y & i_z \\ j_x & j_y & j_z \end{pmatrix} \cdot \left( \overline{\mathbf{s}}_0 + \sum_{i=1}^{\overline{m}} \overline{p}_i \, \overline{\mathbf{s}}_i \right) \tag{9}$$

where $(i_x, i_y, i_z)$, $(j_x, j_y, j_z)$, and the 3D shape parameters $\overline{p}_i$ vary over their allowed values. The projection matrix can be expressed as the sum of 6 matrices:

$$\begin{aligned} \begin{pmatrix} i_x & i_y & i_z \\ j_x & j_y & j_z \end{pmatrix} \;=\; & i_x \begin{pmatrix} 1 & 0 & 0 \\ 0 & 0 & 0 \end{pmatrix} + i_y \begin{pmatrix} 0 & 1 & 0 \\ 0 & 0 & 0 \end{pmatrix} + i_z \begin{pmatrix} 0 & 0 & 1 \\ 0 & 0 & 0 \end{pmatrix} + \\ & j_x \begin{pmatrix} 0 & 0 & 0 \\ 1 & 0 & 0 \end{pmatrix} + j_y \begin{pmatrix} 0 & 0 & 0 \\ 0 & 1 & 0 \end{pmatrix} + j_z \begin{pmatrix} 0 & 0 & 0 \\ 0 & 0 & 1 \end{pmatrix}. \end{aligned} \tag{10}$$

Equation (9) is therefore a linear combination of:

$$\begin{pmatrix} 1 & 0 & 0 \\ 0 & 0 & 0 \end{pmatrix} \cdot \overline{\mathbf{s}}_i, \quad \begin{pmatrix} 0 & 1 & 0 \\ 0 & 0 & 0 \end{pmatrix} \cdot \overline{\mathbf{s}}_i, \quad \begin{pmatrix} 0 & 0 & 1 \\ 0 & 0 & 0 \end{pmatrix} \cdot \overline{\mathbf{s}}_i,$$

$$\begin{pmatrix} 0 & 0 & 0 \\ 1 & 0 & 0 \end{pmatrix} \cdot \bar{\mathbf{s}}_i, \quad \begin{pmatrix} 0 & 0 & 0 \\ 0 & 1 & 0 \end{pmatrix} \cdot \bar{\mathbf{s}}_i, \quad \text{and} \quad \begin{pmatrix} 0 & 0 & 0 \\ 0 & 0 & 1 \end{pmatrix} \cdot \bar{\mathbf{s}}_i \tag{11}$$

for $i = 0, 1, \ldots, \overline{m}$. The shape variation of the 3D model can therefore be represented by the following 2D shape vectors:

$$\mathbf{s}_{6*i+1} = \begin{pmatrix} 1 & 0 & 0 \\ 0 & 0 & 0 \end{pmatrix} \cdot \bar{\mathbf{s}}_i, \quad \mathbf{s}_{6*i+2} = \begin{pmatrix} 0 & 1 & 0 \\ 0 & 0 & 0 \end{pmatrix} \cdot \bar{\mathbf{s}}_i, \quad \mathbf{s}_{6*i+3} = \begin{pmatrix} 0 & 0 & 0 \\ 0 & 0 & 1 \end{pmatrix} \cdot \bar{\mathbf{s}}_i,$$
$$\mathbf{s}_{6*i+4} = \begin{pmatrix} 0 & 0 & 0 \\ 1 & 0 & 0 \end{pmatrix} \cdot \bar{\mathbf{s}}_i, \quad \mathbf{s}_{6*i+5} = \begin{pmatrix} 0 & 0 & 0 \\ 0 & 1 & 0 \end{pmatrix} \cdot \bar{\mathbf{s}}_i, \quad \mathbf{s}_{6*i+6} = \begin{pmatrix} 0 & 0 & 0 \\ 0 & 0 & 1 \end{pmatrix} \cdot \bar{\mathbf{s}}_i \tag{12}$$

for $i = 0, 1, \ldots, \overline{m}$. In total as many as $m = 6 \times (\overline{m} + 1)$ 2D shape vectors may be needed to model the same shape variation as the 3D model with only $\overline{m}$ 3D shape vectors. Although many more shape vectors may be needed, the main point is that 2D models can represent any phenomena that 3D models can. (Note that although theoretically more than 6 times as many 2D shape vectors may be needed, in practice not that many are required. Typically 2-3 times as many are needed.)

## 3.2 3D Realizability of 2D Model Instances

If it takes 6 times as many parameters to represent a certain phenomenon with an 2D model than it does with the corresponding 3D model, the 2D model must be able to generate a large number of model instances that are impossible to generate with the 3D model. In effect, the 2D model has too much representational power. It describes the phenomenon in question, plus a variety of other shapes that are "physically unrealizable." If the parameters of the 2D model are chosen so that the orthogonality constraints on the corresponding 3D projection axes **i** and **j** do not hold, the 2D model instance is not realizable with the 3D model. An example is presented in Figure 1.

The scene in Figure 1 consists of a static cube (7 visible vertices) and 3 moving points (diamond, triangle, and square.) The 3 points can move along the three axes at the same, non-constant speed. The 3D shape of the scene $\bar{\mathbf{s}}$ is composed of a base shape $\bar{\mathbf{s}}_0$ and a single 3D shape vector

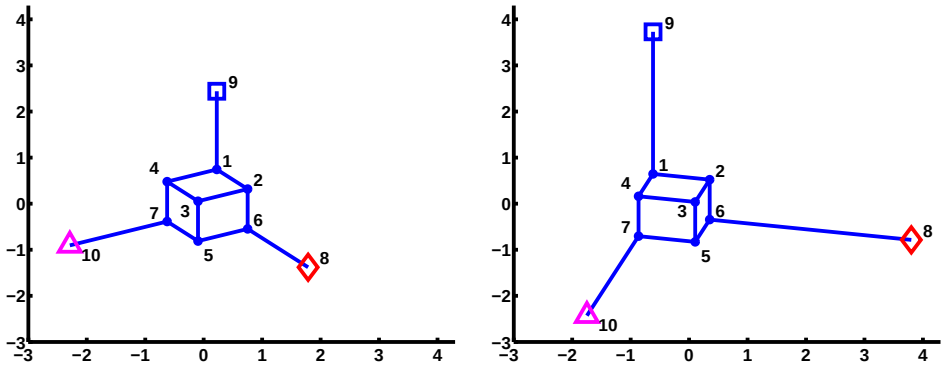


**Figure 1:** A scene consisting of a static cube and 3 points moving along fixed directions. (a) The base configuration. (b) The cube viewed from a different direction with the 3 points (8,9,10) moved.

$\bar{\mathbf{s}}_1$. The base shape $\bar{\mathbf{s}}_0$ correspond to the static cube and the initial locations of the three moving points. The 3D shape vector $\bar{\mathbf{s}}_1$ corresponds to the motion of the three moving points (8,9,10).

We randomly generated 60 sets of shape parameters $\overline{p}_1$ and camera projection matrices $\mathbf{P}$. We then used these to synthesize the 2D shapes of 60 3D model instances. We then computed the 2D shape model by performing PCA on the 60 2D shapes. The result consists of 12 shape vectors, confirming the result above that as many as $6 \times (\overline{m} + 1)$ 2D shape vectors might be required.

The resulting 2D shape model can generate shapes that are impossible to generate with the 3D model. One concrete example is the base 2D shape $\mathbf{s}_0$. In our experiment, $\mathbf{s}_0$ turns out to be:

$$\begin{pmatrix} -0.194 & -0.141 & -0.093 & -0.146 & -0.119 & -0.167 & -0.172 & -0.027 & 0.520 & 0.539 \\ 0.280 & 0.139 & 0.036 & 0.177 & -0.056 & 0.048 & 0.085 & -1.013 & 0.795 & -0.491 \end{pmatrix}. \tag{13}$$

To show that $s_0$ is not a 3D model instance, we first note that $\mathbf{s}_0$ can be *uniquely* decomposed into:

$$\mathbf{s}_0 = \begin{pmatrix} 0.053 & 0.026 & 0.048 \\ -0.141 & 0.091 & -0.106 \end{pmatrix} \bar{\mathbf{s}}_0 + \begin{pmatrix} 0.087 & 0.688 & 0.663 \\ -0.919 & 0.424 & -0.473 \end{pmatrix} \bar{\mathbf{s}}_1. \tag{14}$$

The projection matrices in this expression are not legitimate scaled orthographic matrices (i.e. composed of two equal length, orthogonal vectors). Therefore, $\mathbf{s}_0$ is not a valid 3D model instance.

### 3.3 Summary

Although we have shown that a 2D model can be used to model a 3D face just as well as a 3D model, the parameterization is less compact and the 2D model will be able to generate "physically unrealizable" face instances; i.e. not all 2D face model instances are valid projections of 3D faces. As a result, the fitting of 2D face models is more prone to local minima and so is less robust. See Section 5.5 for empirical results that validate this claim. One additional benefit of 3D models is that the parameterization is more natural. The head pose is contained in the scaled orthographic camera matrix $\mathbf{P}$ rather than being confused with the non-rigid face motion in the 2D shape model.

## 4 Construction

Usually 2D face models are constructed from 2D image data and 3D face models from 3D range scans. In Section 4.1 we show how a linear non-rigid structure-from-motion algorithm [Xiao *et al.*, 2004b] can be used to construct a 3D face model from 2D data in the form of a collection of 2D model fitting results. In Section 4.2 we show how a 3D model can be projected into 2D and describe how such a procedure is useful for building 2D models that better model rotated faces.

### 4.1 Constructing a 3D Model from 2D Fitting Data

Suppose we have a 2D AAM, a collection of images of one or more faces $I^t(\mathbf{u})$ for $t = 0, \ldots, N$, have fit the 2D AAM to each image, and that the 2D AAM shape parameters in image $I^t(\mathbf{u})$ are $\mathbf{p}^t = (p_1^t, \ldots, p_m^t)^{\mathrm{T}}$. Using Equation (2) we can then compute the 2D AAM shape vector $\mathbf{s}^t$:

$$\mathbf{s}^t = \begin{pmatrix} u_1^t & u_2^t & \ldots & u_n^t \\ v_1^t & v_2^t & \ldots & v_n^t \end{pmatrix} \tag{15}$$

for $t = 0, \ldots, N$. A variety of non-rigid structure-from-motion algorithms have been proposed to convert the feature points in Equation (15) into a 3D shape model. Torresani et al. proposed an algorithm to simultaneously reconstruct the non-rigid 3D shape and camera projection matrices

[Torresani *et al.*, 2001]. This trilinear optimization involves three types of unknowns, 3D shape vectors, shape parameters, and projection matrices. At each step, two of the unknowns are fixed and the third refined. Brand proposed a similar non-linear optimization method [Brand, 2001]. Both of these methods only use the usual orthonormality constraints on the projection matrices [Tomasi and Kanade, 1992]. In [Xiao *et al.*, 2004b] we proved that only enforcing the orthonormality constraints in a linear algorithm is ambiguous and demonstrated that it can lead to an incorrect solution. We now outline how our linear algorithm [Xiao *et al.*, 2004b] can be used to compute 3D shape modes from the 2D AAM fitting data in Equation (15). Any of the other algorithms mentioned above could be used instead, although they do not have the advantage of a linear solution. Since they are large non-linear optimizations, they require good initial estimates to converge.

We begin by stacking the 2D AAM fitting data from Equation (15) into a measurement matrix:

$$W = \begin{pmatrix} u_1^0 & u_2^0 & \dots & u_n^0 \\ v_1^0 & v_2^0 & \dots & v_n^0 \\ \vdots & \vdots & \vdots & \vdots \\ u_1^N & u_2^N & \dots & u_n^N \\ v_1^N & v_2^N & \dots & v_n^N \end{pmatrix}. \tag{16}$$

If this data can be explained by $\overline{m}$ 3D shape modes, the matrix $W$ can be factored into:

$$W = MB = \begin{pmatrix} \mathbf{P}^0 & p_1^0\,\mathbf{P}^0 & \dots & p_{\overline{m}}^0\,\mathbf{P}^0 \\ \mathbf{P}^1 & p_1^1\,\mathbf{P}^1 & \dots & p_{\overline{m}}^1\,\mathbf{P}^1 \\ \vdots & \vdots & \vdots & \vdots \\ \mathbf{P}^N & p_1^N\,\mathbf{P}^N & \dots & p_{\overline{m}}^N\,\mathbf{P}^N \end{pmatrix} \begin{pmatrix} \overline{\mathbf{s}}_0 \\ \vdots \\ \overline{\mathbf{s}}_{\overline{m}} \end{pmatrix} \tag{17}$$

where each $\mathbf{P}^i$, $i = 0, \dots, N$ is a $2 \times 3$ projection matrix (see Equation (7) for a definition), $M$ is a $2(N+1) \times 3(\overline{m}+1)$ scaled projection matrix, and $B$ is a $3(\overline{m}+1) \times n$ shape matrix (setting the number of 3D shape model vertices $\overline{n}$ equal to the number of AAM vertices $n$.) Since $\overline{m}$ is the number of 3D shape vectors, it is usually small and the rank of $W$ is at most $3(\overline{m}+1)$.

We perform a Singular Value Decomposition (SVD) on $W$ and factorize it into the product of a $2(N+1) \times 3(\overline{m}+1)$ matrix $\tilde{M}$ and a $3(\overline{m}+1) \times n$ matrix $\tilde{B}$. This decomposition is not unique. It is only determined up to a linear transformation. Any non-singular $3(\overline{m}+1) \times 3(\overline{m}+1)$ matrix $G$ and its inverse $G^{-1}$ could be inserted between $\tilde{M}$ and $\tilde{B}$ and their product would still equal $W$. The scaled projection matrix $M$ and the shape vector matrix $B$ are then given by:

$$M = \tilde{M} \cdot G, \qquad B = G^{-1} \cdot \tilde{B} \tag{18}$$

where $G$ is a corrective matrix. The first step in solving for $G$ is to impose the usual orthonormality constraints matrices [Tomasi and Kanade, 1992]. If we represent $G$ as the columns $G = (g_0 \cdots g_{\overline{m}})$ where $g_k, k = 0, \ldots, \overline{m}$ are $3(\overline{m}+1) \times 3$ matrices, the left half of Equation (18) takes the form:

$$\tilde{M} \cdot g_k = \begin{pmatrix} p_k^0 \, \mathbf{P}^0 \\ p_k^1 \, \mathbf{P}^1 \\ \vdots \\ p_k^N \, \mathbf{P}^N \end{pmatrix}, \quad k = 0, \ldots, \overline{m}. \tag{19}$$

Denote $g_k g_k^T$ by $Q_k$. Using the orthogonality properties of $\mathbf{P}^i$ outlined in Section 2.2 we have:

$$\tilde{M}_{2i+1} Q_k \tilde{M}_{2i+1}^T = \tilde{M}_{2i+2} Q_k \tilde{M}_{2i+2}^T \tag{20}$$

$$\tilde{M}_{2i+1} Q_k \tilde{M}_{2i+2}^T = 0 \tag{21}$$

for $i = 0, \ldots, N$, and where $\tilde{M}_i$ is the $i_{th}$ row of $\tilde{M}$. Equations (20) and (21) provide $2(N+1)$ linear constraints on the symmetric matrix $Q_k$, which consists of $(9(\overline{m}+1)^2 + 3(\overline{m}+1))/2$ unknowns. In [Xiao *et al.*, 2004b], however, we proved that even if $2(N+1) \geq (9(\overline{m}+1)^2 + 3(\overline{m}+1))/2$, these orthonormality constraints are not sufficient to determine $Q_k$.

Although the 3D shape modes span a unique shape space, the basis of the space is not unique. Any non-singular linear transformation of the shape vectors yields a new set of shape vectors. We

therefore need an additional set of constraints. Without loss of generality, we can assume that the 3D shapes in the first $(\overline{m}+1)$ frames are independent[1] and treat them as the 3D shape basis. Equivalently, we can specify the shape parameters in the first $(\overline{m}+1)$ frames to be:

$$\begin{aligned} \overline{p}_i^i &= \frac{1}{|\mathbf{P}^i|} \quad \text{for } i = 0, \ldots, \overline{m} \\ \overline{p}_j^i &= 0 \quad \text{for } i, j = 0, \ldots, \overline{m},\ i \neq j \end{aligned} \tag{22}$$

where $|\mathbf{P}^i| = i_x^i i_x^i + i_y^i i_y^i + i_z^i i_z^i$. See Equation (7) in Section 2.2 for the definition of $\mathbf{P}$. Combining these constraints with Equation (19) leads to another set of linear constraints on $Q_k$:

$$\tilde{M}_{2i+1} Q_k \tilde{M}_{2j+1}^T = \begin{cases} 1 & \text{if } i = j = k \\ 0 & \text{if } i \neq k \end{cases} \tag{23}$$

$$\tilde{M}_{2i+2} Q_k \tilde{M}_{2j+2}^T = \begin{cases} 1 & \text{if } i = j = k \\ 0 & \text{if } i \neq k \end{cases} \tag{24}$$

$$\tilde{M}_{2i+1} Q_k \tilde{M}_{2j+2}^T = 0 \quad \text{if } i \neq k \text{ or } i = j = k \tag{25}$$

$$\tilde{M}_{2i+2} Q_k \tilde{M}_{2j+1}^T = 0 \quad \text{if } i \neq k \text{ or } i = j = k \tag{26}$$

where $i = 0, \ldots, \overline{m}$ and $j = 0, \ldots, N$. Enforcing the (roughly) $4(\overline{m}+1)(N+1)$ linear constraints in Equations (23)–(26) and the $2(N+1)$ linear constraints in Equations (20) and (21) leads to a closed-form solution for $Q_k$. Since $Q_k = g_k g_k^T$ we can solve for $g_k$ using SVD [Tomasi and Kanade, 1992]. We can finally recover $M$ and $B$ using Equation (18).

We illustrate the computation of a 3D shape model from a 2D shape model in Figure 2. We first constructed a 2D AAM for 5 people using approximately 20 training images of each person. In Figure 2(A) we include the AAM mean 2D shape $\mathbf{s}_0$ and the first 3 (of 8) 2D shape variation modes $\mathbf{s}_1$, $\mathbf{s}_2$, and $\mathbf{s}_3$. In Figure 2(B) we include the AAM mean appearance $A_0$ and an illustration of the appearance variation. Instead of displaying the appearance modes themselves, we display

[1] If the first $(\overline{m}+1)$ shape vectors are not independent, we can find $(\overline{m}+1)$ frames in which the shapes are independent by examining the singular values of their image projections. We can then reorder the images.

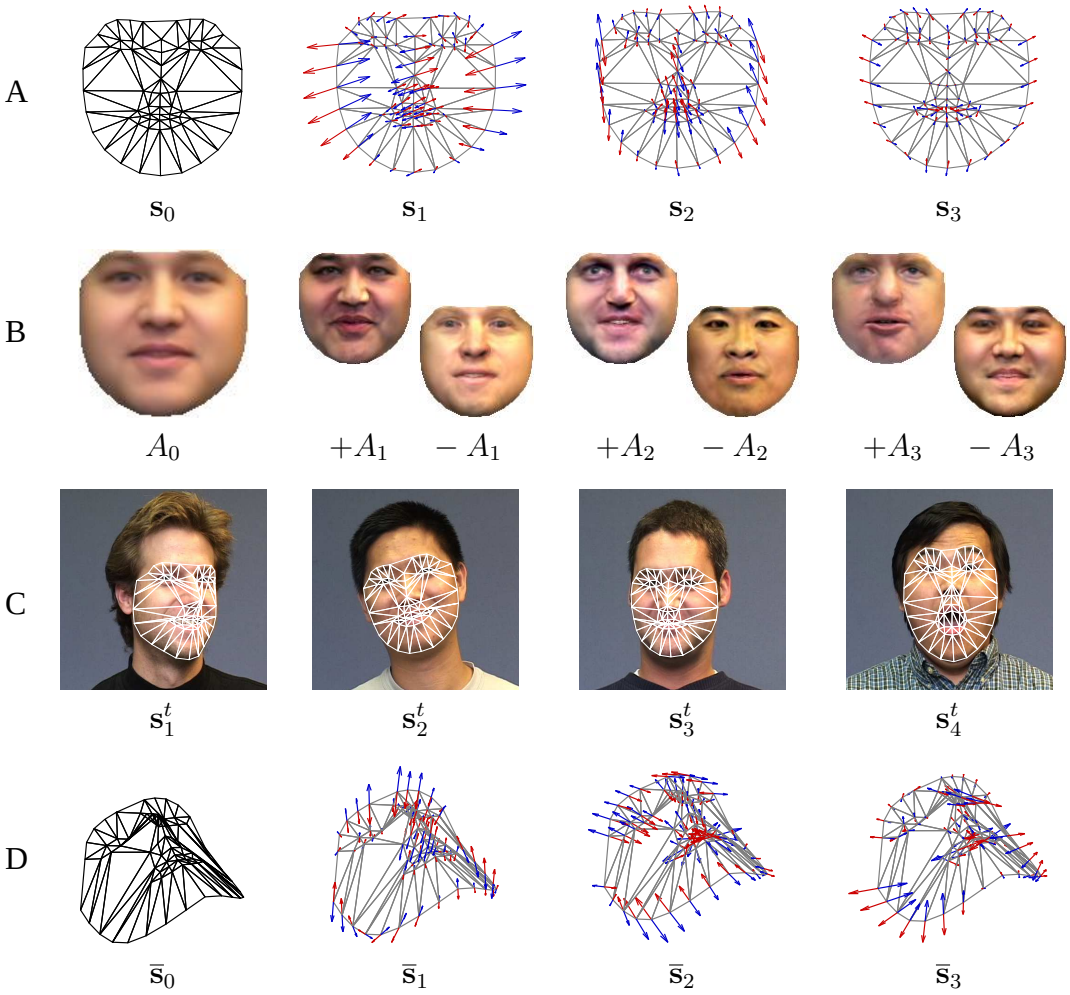


**Figure 2:** Model and Dataset 1: Constructing a 3D model from 2D data for a 5 person model. (A) The 2D AAM shape variation. (B) The 2D AAM appearance variation. (C) Example frames of the AAM being used to track 4 of the 5 subjects, the input to our algorithm. (D) The output of our algorithm, the mean 3D shape $\bar{\mathbf{s}}_0$ and the first 3 (of 4) 3D shape modes $\bar{\mathbf{s}}_1$, $\bar{\mathbf{s}}_2$, and $\bar{\mathbf{s}}_3$.

the result of adding and subtracting the first 3 (of 40) modes to the mean appearance. For example, $+A_1$ denotes the addition of the first appearance mode to the mean appearance; i.e. $A_0 + A_1$. Next we use the 2D AAM to track short 180 frame videos of each of the 5 subjects to generate the input to the non-rigid structure-from-motion algorithm. One example frame for 4 of the 5 subjects is included in Figure 2(C). The results of our 3D model construction algorithm are shown in Figure 2(D). In particular, we display the mean 3D shape $\bar{\mathbf{s}}_0$ and the first 3 (of 4) 3D shape modes $\bar{\mathbf{s}}_1$, $\bar{\mathbf{s}}_2$, and $\bar{\mathbf{s}}_3$, with the 3D shape modes illustrated as arrows on the mean shape.

Similar results for a different model and dataset are included in Figure 3. In this case, the 2D

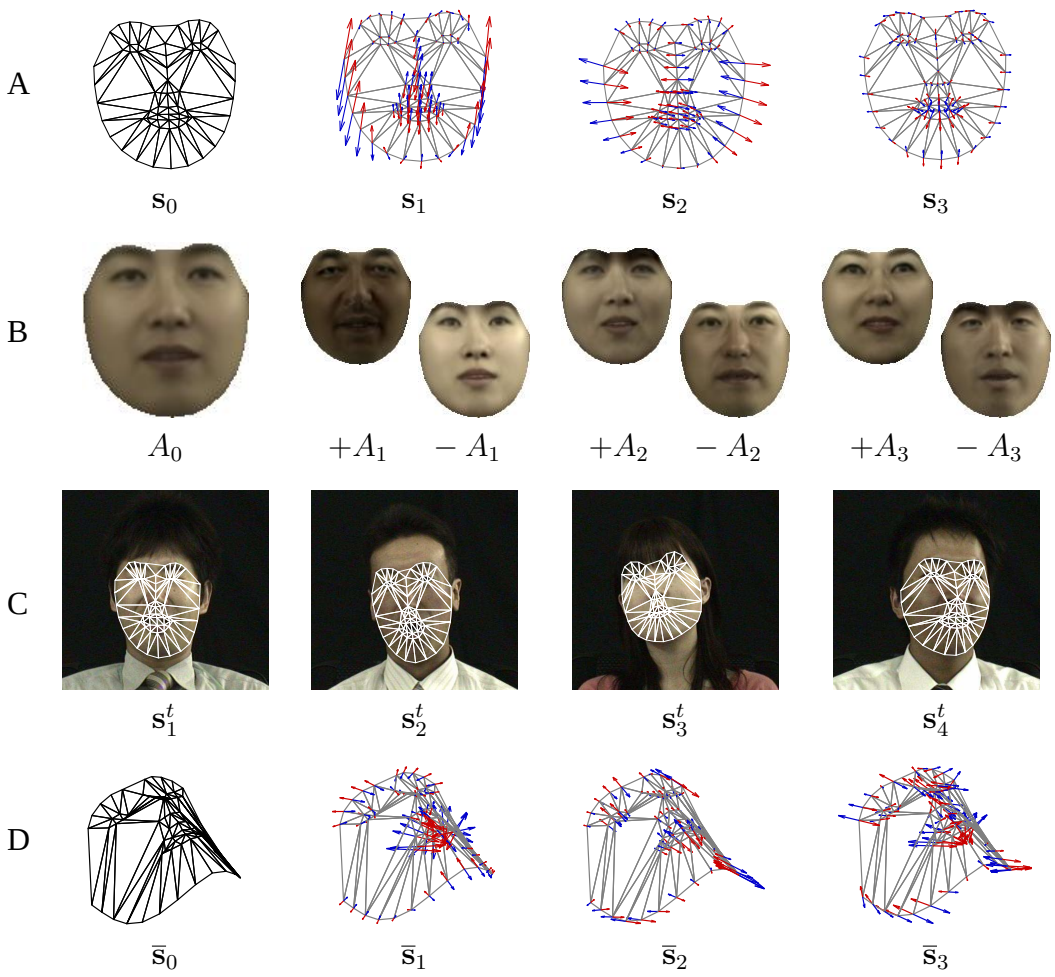


**Figure 3:** Model and Dataset 2: Constructing a 3D model from 2D data. (A) The 2D AAM shape variation. (B) The 2D AAM appearance variation. (C) Example frames of the AAM being used to track 4 of the subjects, the input to our algorithm. (D) The output of our algorithm, the mean 3D shape $\bar{\mathbf{s}}_0$ and the first 3 (of 4) 3D shape modes $\bar{\mathbf{s}}_1$, $\bar{\mathbf{s}}_2$, and $\bar{\mathbf{s}}_3$.

AAM is constructed from 20–30 training images of each of 9 subjects, has 9 2D shape modes, and 59 2D appearance modes. We use the 2D AAM to track 150 frame videos for 9 subjects. The output of our algorithm consists of a 3D model with 4 3D shape modes, of which we show the mean 3D shape $\bar{\mathbf{s}}_0$ and the first 3 modes $\bar{\mathbf{s}}_1$, $\bar{\mathbf{s}}_2$, and $\bar{\mathbf{s}}_3$ in Figure 3(D).

## 4.2 Constructing a 2D Model from a 3D Model

Constructing a 2D model from a 3D model is obviously easier than the other way around. We actually already did this in Section 3.2 when we were searching for a "physically unrealizable"

2D model instance. We simply take the 3D model, generate a large number of model instances (which are 2D shape vectors), and then construct the 2D model in the usual manner. The 3D model parameters and scaled orthographic projection matrix parameters can either be sampled systematically or randomly. In practice, we use a systematic sampling of the 2D (yaw/pitch) pose space and non-rigid shape space. (Scale, roll, and translation do not need to be sampled as they are modeled by the 2D similarity transformation.) In Figure 4 we include 15 (of 465) example 3D model instances generated from the 4-dimensional 3D shape model in Figure 2(D). These 465

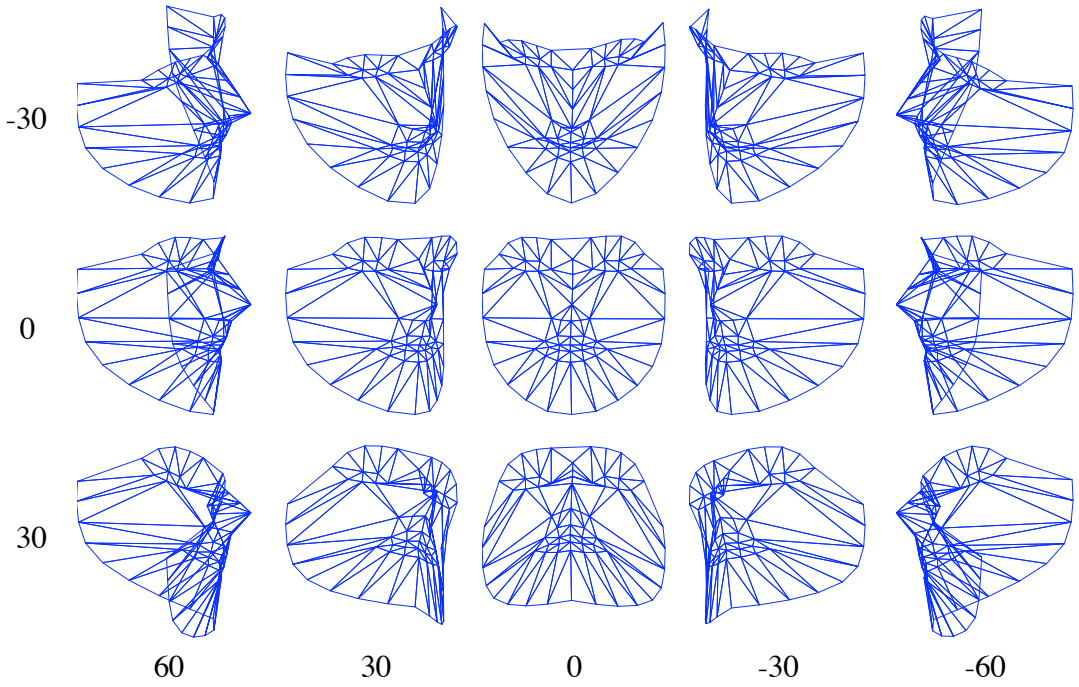


**Figure 4:** 3D model instances generated using the 3D model in Figure 2(D). The pose is sampled systematically and the non-rigid shape randomly. These model instances are a subset of a set of 465 used to re-generate the 2D shape model in Figure 2(A), and which is evaluated in Figure 5.

training examples were then used to re-generate the 8-dimensional 2D shape model in Figure 2(A). The result is a new 2D shape model with 9 modes.

A natural question, however, is: "why would you ever want to convert a 3D model into a 2D model?" One possibility is when working with either a 2D or a 2D+3D model [Xiao *et al.*, 2004a] (to obtain real-time fitting speed) and trying to build models that can model the face across large pose variation. Although algorithms have been proposed to build 2D AAMs in the presence of

occlusion caused by large pose variation in the training set [Gross *et al.*, 2004], another way to build a 2D AAM than can model large pose variation is to: (1) build a normal 2D model using training data with no occlusion and so limited pose variation, (2) convert the 2D model into a 3D model using the approach in Section 4.1, and finally (3) convert the resulting 3D model back into a 2D model using an extending sampling of the camera matrix to model increased pose variation and self occlusion. Some results of performing this three-step procedure are included in Figure 5. In particular, for 3 different head poses (0 degrees yaw, 30 degrees yaw, and 60 degrees yaw) we

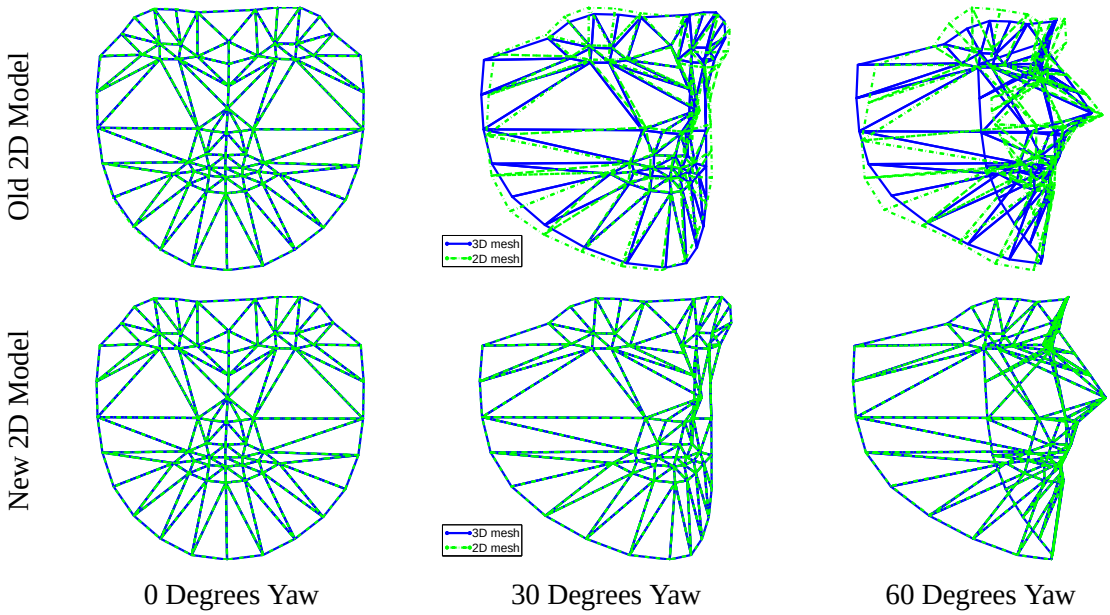


**Figure 5:** An example of 2D model construction from a 3D model. We display 3D model instances (solid blue line) and the closest 2D model instance (dashed green line) for 3 different head poses. We display the closest 2D model instances for the original 2D model (top row) and the new 2D model computed from the 3D model (bottom row). The results show that the new 2D model computed from the 3D model is better able to model faces at high degrees of pose variation.

display the 3D model instance (solid blue line) and the closest 2D model instance (dashed green line) for both the original 2D model and the new 2D model computed from the 3D model. The results show that the new 2D model computed from the 3D model is better able to model faces at high degrees of pose variation than the original 2D model was able to.

### 4.3 Summary

We have shown that 3D models can be constructed from 2D data, and vica versa. In particular, 3D models such as 3D Morphable Models [Blanz and Vetter, 1999] and 2D+3D Active Appearance Models [Xiao *et al.*, 2004a] can be constructed from images collected with the same cameras that will be used in the final application. The training data is therefore more closely matched to the application data, a property that generally results in better (fitting and application) performance. On the other hand, one residual advantage of building 3D models from 3D range scans is that it is currently easier to build dense 3D models from range scans (although the non-rigid structure-from-motion algorithms described in this section could obviously operate on dense sets of features.) Techniques have been proposed for computing dense 3D models from 2D data, however, currently the models constructed in this manner do not match the quality of 3D models constructed from 3D range scans. This is an active area of research and so the gap may soon be closed.

## 5 Fitting

In [Baker and Matthews, 2001, Matthews and Baker, 2004] we proposed a real-time algorithm for fitting 2D Active Appearance Models. On the other hand, Romdhani and Vetter recently presented an algorithm for fitting 3D Morphable Models that operates at around 30 seconds per frame [Romdhani and Vetter, 2003]; i.e. thousands of times slower. In this section, we investigate why fitting 3D models is less efficient than fitting 2D models. We begin in Section 5.1 with a brief review of our real-time algorithm for fitting 2D AAMs. This algorithm is based on the inverse compositional image alignment algorithm [Baker and Matthews, 2004]. In Section 5.2 we present a brief argument of why the inverse compositional algorithm does not generalize naturally to 3D shape models [Baker *et al.*, 2004b]. In Section 5.3, we propose a work around to this problem, a real-time algorithm for fitting a 3D model that operates by fitting the 3D model indirectly through a 2D model [Xiao *et al.*, 2004a]. After a qualitative evaluation of the 3D fitting algorithm in Section 5.4, we present a quantitative comparison of the robustness, rate of convergence, and computational

cost of the 2D and 3D fitting algorithms in Sections 5.5–5.6.

## 5.1 Efficient 2D Model Fitting

The goal of fitting a 2D AAM [Matthews and Baker, 2004] is to minimize:

$$\sum_{\mathbf{u}\in\mathbf{s}_0}\left[A_0(\mathbf{u})+\sum_{i=1}^{l}\lambda_i A_i(\mathbf{u})-I(\mathbf{N}(\mathbf{W}(\mathbf{u};\mathbf{p});\mathbf{q}))\right]^2 \tag{27}$$

*simultaneously* with respect to the shape $\mathbf{p}$, appearance $\boldsymbol{\lambda}$, and normalization $\mathbf{q}$ parameters. The algorithm in [Matthews and Baker, 2004] uses the "Project Out" algorithm [Hager and Belhumeur, 1998] (described in more detail with an empirical evaluation that highlights some limitations of the algorithm in [Baker *et al.*, 2003]) to break the optimization into two steps. We first optimize:

$$\|A_0(\mathbf{u})-I(\mathbf{N}(\mathbf{W}(\mathbf{u};\mathbf{p});\mathbf{q}))\|^2_{\mathrm{span}(A_i)^\perp} \tag{28}$$

with respect to $\mathbf{p}$ and $\mathbf{q}$, where $\|\cdot\|^2_{\mathrm{span}(A_i)^\perp}$ denotes the square of the L2 norm of the vector projected into orthogonal complement of the linear subspace spanned by the vectors $A_1,\ldots,A_l$. Afterwards, we solve for the appearance parameters using the linear closed-form solution:

$$\lambda_i \;=\; -\sum_{\mathbf{u}\in\mathbf{s}_0} A_i(\mathbf{u})\cdot[A_0(\mathbf{u})-I(\mathbf{N}(\mathbf{W}(\mathbf{u};\mathbf{p});\mathbf{q}))] \tag{29}$$

where the shape $\mathbf{p}$ and normalization $\mathbf{q}$ parameters are the result of the previous optimization. Equation (29) assumes that the appearance vectors $A_i(\mathbf{u})$ have been orthonormalized.

In [Matthews and Baker, 2004] we showed how to use the inverse compositional algorithm [Baker and Matthews, 2004] to optimize the expression in Equation (28) with respect to the shape parameters $\mathbf{p}$ and the normalization parameters $\mathbf{q}$. The main technical contribution allowing the use of the inverse compositional algorithm is a proof that approximately minimizing:

$$\|A_0(\mathbf{u})-I(\mathbf{N}(\mathbf{W}(\mathbf{u};\mathbf{p}+\Delta\mathbf{p});\mathbf{q}+\Delta\mathbf{q}))\|^2_{\mathrm{span}(A_i)^\perp} \tag{30}$$

with respect to $\Delta\mathbf{p}$ and $\Delta\mathbf{q}$, and then updating $\mathbf{p} \leftarrow \mathbf{p} + \Delta\mathbf{p}$ and $\mathbf{q} \leftarrow \mathbf{q} + \Delta\mathbf{q}$, is the same to a first order approximation as approximately minimizing:

$$\|A_0(\mathbf{N}(\mathbf{W}(\mathbf{u};\Delta\mathbf{p});\Delta\mathbf{q})) - I(\mathbf{N}(\mathbf{W}(\mathbf{u};\mathbf{p};\mathbf{q}))\|^2_{\mathrm{span}(A_i)^\perp} \tag{31}$$

with respect to $\Delta\mathbf{p}$ and $\Delta\mathbf{q}$, and then updating the warp using the inverse compositional update:

$$\mathbf{N}(\mathbf{W}(\mathbf{u};\mathbf{p});\mathbf{q}) \;\leftarrow\; \mathbf{N}(\mathbf{W}(\mathbf{u};\mathbf{p});\mathbf{q}) \circ \mathbf{N}(\mathbf{W}(\mathbf{u};\Delta\mathbf{p});\Delta\mathbf{q})^{-1}. \tag{32}$$

The algorithm itself then consists of iterating two main steps. The first step computes:

$$\begin{pmatrix} \Delta\mathbf{p} \\ \Delta\mathbf{q} \end{pmatrix} \;=\; -H_{2\mathrm{D}}^{-1} \begin{pmatrix} \Delta\mathbf{p}_{\mathrm{SD}} \\ \Delta\mathbf{q}_{\mathrm{SD}} \end{pmatrix} \tag{33}$$

where the steepest descent parameter updates $\begin{pmatrix} \Delta\mathbf{p}_{\mathrm{SD}} \\ \Delta\mathbf{q}_{\mathrm{SD}} \end{pmatrix}$ are:

$$\begin{pmatrix} \Delta\mathbf{p}_{\mathrm{SD}} \\ \Delta\mathbf{q}_{\mathrm{SD}} \end{pmatrix} \;=\; \sum_{\mathbf{u}\in\mathbf{s}_0} \left[\mathbf{SD}_{2\mathrm{D}}(\mathbf{u})\right]^{\mathrm{T}} \left[A_0(\mathbf{u}) - I(\mathbf{N}(\mathbf{W}(\mathbf{u};\mathbf{p});\mathbf{q}))\right]. \tag{34}$$

In this expression, the steepest descent images $\mathbf{SD}_{2\mathrm{D}}(\mathbf{u})$ are the concatenation of:

$$\mathbf{SD}_{2\mathrm{D}}(\mathbf{u}) = \left( \left[\nabla A_0 \frac{\partial \mathbf{N}\circ\mathbf{W}}{\partial \mathbf{p}}\right]_{\mathrm{span}(A_i)^\perp} \left[\nabla A_0 \frac{\partial \mathbf{N}\circ\mathbf{W}}{\partial \mathbf{q}}\right]_{\mathrm{span}(A_i)^\perp} \right) \tag{35}$$

one for the shape, and one for the normalization parameters. The Hessian matrix $H_{2\mathrm{D}}$ is:

$$H_{2\mathrm{D}} \;=\; \sum_{\mathbf{u}\in\mathbf{s}_0} \left[\mathbf{SD}_{2\mathrm{D}}(\mathbf{u})\right]^{\mathrm{T}} \mathbf{SD}_{2\mathrm{D}}(\mathbf{u}). \tag{36}$$

The second step consists of updating the warp with the inverse compositional update in Equa-

tion (32). The inverse compositional algorithm obtains its efficiency from the fact that Equations (35) and (36) can be pre-computed for any given model. The Hessian can even be pre-multiplied by the steepest descent images. (This pre-computation is omitted in the presentation above to allow easier explanation of the extension of the algorithm in Section 5.3 below.) All that is left is: (1) a piecewise affine warp to generate $I(\mathbf{N}(\mathbf{W}(\mathbf{u};\mathbf{p});\mathbf{q}))$, (2) an image subtraction to generate $A_0(\mathbf{u}) - I(\mathbf{N}(\mathbf{W}(\mathbf{u};\mathbf{p});\mathbf{q}))$, (3) $m+4$ image dot products where there are $m$ shape and $4$ similarity normalization parameters, and (4) the inverse compositional update to the warp. Although computing the inverse compositional warp update is involved [Matthews and Baker, 2004], it is not computationally demanding because it only requires operations on the mesh, rather than on the images. All four of these steps can be implemented in real-time [Matthews and Baker, 2004].

## 5.2 Invalidity of the 3D Inverse Compositional Algorithm

At this point it is natural to ask whether the inverse compositional algorithm generalizes to 3D models. Unfortunately, the *direct generalization* violates one of the key assumptions made in the proof of correctness [Baker *et al.*, 2004b]. Note, however, that at least two "work-arounds" have been proposed to avoid this problem: (1) the 2D+3D constrained fitting algorithm described in Section 5.3 and (2) the implicit 2D parameterization of [Romdhani and Vetter, 2003] described in Section 5.7. We now briefly outline the argument in [Baker *et al.*, 2004b] of why the inverse compositional algorithm does not generalize to 3D models (described as 2.5D data in [Baker *et al.*, 2004b] to distinguish it from 3D volumetric data such as MRI and CT scans.)

In the proof of equivalence of the forwards and inverse compositional algorithms in [Baker and Matthews, 2004], an assumption is made that:

$$\|A_0(\mathbf{N}(\mathbf{W}(\mathbf{u};\Delta\mathbf{p});\Delta\mathbf{q})) - I(\mathbf{N}(\mathbf{W}(\mathbf{u};\mathbf{p};\mathbf{q}))\|^2_{\mathrm{span}(A_i)^\perp} \;=\; O(\Delta\mathbf{p},\Delta\mathbf{q}). \tag{37}$$

Intuitively, in order to replace gradients of $I$ in the forwards compositional algorithm with gradients of $A_0$ in the inverse compositional algorithm, an assumption is needed that $I$ and $A_0$ are

approximately the same (after compensating for the geometric distortion modeled by the warp $\mathbf{N} \circ \mathbf{W}$ and working in the subspace $\mathrm{span}(A_i)^\perp$.) The assumption in Equation (37) is reasonable in the 2D case. Intuitively, all it says is that the mean appearance matches the image reasonably well after: (1) compensating for the shape deformation and (2) projecting out the appearance variation.

If we generalize Equation (37) to 3D we end up with something like:

$$\left\| A_0(\mathbf{P}(\overline{\mathbf{W}}(\mathbf{x}; \Delta\overline{\mathbf{p}}))) - I(\mathbf{P}(\overline{\mathbf{W}}(\mathbf{x}; \overline{\mathbf{p}}))) \right\|^2_{\mathrm{span}(A_i)^\perp} \; = \; O(\Delta\overline{\mathbf{p}}) \tag{38}$$

where $\overline{\mathbf{W}}(\mathbf{x}; \overline{\mathbf{p}})$ is a 3D warp with 3D shape parameters $\overline{\mathbf{p}}$ using 3D coordinates $\mathbf{x}$ rather than 2D coordinates $\mathbf{u}$, and $\mathbf{P}$ is the scaled orthographic projection from 3D to 2D (for simplicity ignoring the origin offset $(o_u, o_v)^{\mathrm{T}}$.) While it is reasonable to assume that the assumption in Equation (38) holds for 3D points $\mathbf{x}$ on the surface of the head model, the same is not true for points $\mathbf{x}$ away from the surface. See [Baker *et al.*, 2004b] for more explanation of why. Although it might not seem like Equation (38) needs to hold away from the surface in the proof of equivalence, it does. In moving from the 3D forwards compositional algorithm to the 3D inverse compositional algorithm, we effectively need to replace 3D gradients of $I(\mathbf{P}(\mathbf{x}))$ with 3D gradients of $A_0(\mathbf{P}(\mathbf{x}))$. For this to be possible, Equation (38) must hold both for 3D points $\mathbf{x}$ on the surface of the model and for 3D points $\mathbf{x}$ infinitesimally close, but slightly away from the 3D surface.

The argument in this section is meant to be informal. A more complete explanation and an empirical validation is outside the scope of this paper and is covered in other papers [Baker *et al.*, 2004b]. The main point is that whenever the 3D-to-2D projection matrix $\mathbf{P}$ appears *explicitly* in the image part of the model fitting goal, the inverse compositional algorithm is not applicable.

## 5.3 Constrained 3D Fitting

One way to avoid the problem just described is to use both a 2D model and a 3D model. The 2D model is fit to the image subject to the constraints that the 2D model equals the projection of the 3D

model. In essence, the 3D model is fit to the image[2] through the 2D model. The image gradients are 2D, so the inverse compositional algorithm can be used. Imposing the constraints between the 2D and 3D models can be performed without significantly reducing the speed of the algorithm, as we will now show. The result is a real-time 3D model fitting algorithm.

Suppose we have a 2D shape model defined by Equation (2) and a 3D shape model defined by Equation (5). Denote the result of mapping the 2D model into an image with the normalization $\mathbf{N}(\mathbf{u};\mathbf{q})$ by $\mathbf{N}(\mathbf{s};\mathbf{q}) = \mathbf{N}\left(\mathbf{s}_0 + \sum_{i=1}^{m} p_i\,\mathbf{s}_i;\mathbf{q}\right)$. Similarly, denote the projection of the 3D model into the image by $\mathbf{P}\left(\overline{\mathbf{s}}_0 + \sum_{i=1}^{\overline{m}} \overline{p}_i\,\overline{\mathbf{s}}_i\right) + \begin{pmatrix} o_u & \dots & o_u \\ o_v & \dots & o_v \end{pmatrix}$. See Equation (8) in Section 2.2 for a definition of the scaled orthographic image formation model being used in this paper. We can impose the constraints that the projection of the 3D shape model equals the normalized 2D shape model as soft constraints with a large weight $K$ by modifying the fitting goal in Equation (27) to:

$$\sum_{\mathbf{u}\in\mathbf{s}_0}\left[A_0(\mathbf{u}) + \sum_{i=1}^{l}\lambda_i A_i(\mathbf{u}) - I(\mathbf{N}(\mathbf{W}(\mathbf{u};\mathbf{p});\mathbf{q}))\right]^2$$

$$+ K\cdot\left\|\mathbf{P}\left(\overline{\mathbf{s}}_0 + \sum_{i=1}^{\overline{m}}\overline{p}_i\,\overline{\mathbf{s}}_i\right) + \begin{pmatrix} o_u & \dots & o_u \\ o_v & \dots & o_v \end{pmatrix} - \mathbf{N}\left(\mathbf{s}_0 + \sum_{i=1}^{m} p_i\,\mathbf{s}_i;\mathbf{q}\right)\right\|^2. \tag{39}$$

The first term in Equation (39) is the 2D fitting goal of Equation (27). The second term imposes the constraint that the projection of the 3D model equals the normalized 2D shape. The optimization is performed simultaneously with respect to the 2D shape parameters $\mathbf{p}$, the 2D normalization parameters $\mathbf{q}$, the appearance parameters $\boldsymbol{\lambda}$, the 3D shape parameters $\overline{\mathbf{p}}$, the parameters of the scaled orthographic projection matrix $\mathbf{P}$ (see below for more details), and the offset to the origin $(o_u, o_v)^{\mathrm{T}}$. In the limit $K \to \infty$ the constraints become hard. In practice, a suitably large value for $K$ results in the system being solved approximately as though the constraints are hard. Finally note

[2] A quick note on this interpretation of the algorithm. We optimize a function $F^2(\mathrm{2D}) + K\cdot G^2(\mathrm{2D},\mathrm{3D})$ where $F$ models how well the 2D model matches the image, $G$ models how well the 2D model matches the projection of the 3D model, and $K$ is a large weight. One interpretation of optimizing this function is that $G$ is a just prior on $F$. If $G$ is such that given 3D, there is just a single set 2D such that $G^2(\mathrm{2D},\mathrm{3D}) = 0$ (which is the case for us), then an equally valid interpretation of the algorithm is that $F$ is optimized with respect to the 3D parameters through the 2D ones.

that for the constraints in the second term of Equation (39) to make sense, we need the argument in Section 3.1 to show that the projection of any 3D shape can also be generated by a 2D shape model. In a sense, Section 3.1 is a "proof of correctness" of this formulation of 3D model fitting.

As above, we use the "Project Out" algorithm [Hager and Belhumeur, 1998] and first optimize:

$$\|A_0(\mathbf{u}) - I(\mathbf{N}(\mathbf{W}(\mathbf{u};\mathbf{p});\mathbf{q}))\|^2_{\mathrm{span}(A_i)^\perp}$$

$$+ K \cdot \left\| \mathbf{P}\left(\overline{\mathbf{s}}_0 + \sum_{i=1}^{\overline{m}} \overline{p}_i\, \overline{\mathbf{s}}_i\right) + \begin{pmatrix} o_u & \ldots & o_u \\ o_v & \ldots & o_v \end{pmatrix} - \mathbf{N}\left(\mathbf{s}_0 + \sum_{i=1}^{m} p_i\, \mathbf{s}_i;\mathbf{q}\right) \right\|^2 . \tag{40}$$

with respect to $\mathbf{p}$, $\mathbf{q}$, $\overline{\mathbf{p}}$, $\mathbf{P}$, and $(o_u, o_v)^{\mathrm{T}}$. Afterwards, we solve for $\boldsymbol{\lambda}$ using Equation (29).

In [Baker *et al.*, 2004a] we showed how to extend the inverse compositional algorithm to allow constraints on the warp parameters. Equation (40) is of the form:

$$G(\mathbf{p};\mathbf{q}) + \; K \cdot \sum_{t=u,v} \sum_{i=1}^{n} F^2_{t_i}(\mathbf{p};\mathbf{q};\overline{\mathbf{p}};\mathbf{P};o_u;o_v) \tag{41}$$

where $G(\mathbf{p};\mathbf{q}) = \|A_0(\mathbf{u}) - I(\mathbf{N}(\mathbf{W}(\mathbf{u};\mathbf{p});\mathbf{q}))\|^2_{\mathrm{span}(A_i)^\perp}$, $F^2_{v_i}(\mathbf{p};\mathbf{q};\overline{\mathbf{p}};\mathbf{P};o_u;o_v)$ is the component of the L2 norm in the second term corresponding to vertex $u_i$, and $F^2_{v_i}(\mathbf{p};\mathbf{q};\overline{\mathbf{p}}\mathbf{P};o_u;o_v)$ is the component corresponding to vertex $v_i$. In the usual forwards additive (Lucas-Kanade) algorithm [Baker and Matthews, 2004], we solve for updates the the parameters $\Delta\mathbf{p}$ and $\Delta\mathbf{q}$ that approximately minimize $G(\mathbf{p}+\Delta\mathbf{p};\mathbf{q}+\Delta\mathbf{q})$. With the inverse compositional algorithm, however, (see [Baker *et al.*, 2004a]) we effectively solve for updates to the parameters that approximately minimize:

$$G(\mathbf{p}+\mathbf{J}_\mathbf{p}\Delta\mathbf{p};\mathbf{q}+\mathbf{J}_\mathbf{q}\Delta\mathbf{q}) \tag{42}$$

where to a first order approximation:

$$\mathbf{N}(\mathbf{W}(\mathbf{u};\mathbf{p}+\mathbf{J}_\mathbf{p}\Delta\mathbf{p});\mathbf{q}+\mathbf{J}_\mathbf{q}\Delta\mathbf{q}) \;\approx\; \mathbf{N}(\mathbf{W}(\mathbf{u};\mathbf{p});\mathbf{q}) \circ \mathbf{N}(\mathbf{W}(\mathbf{u};\Delta\mathbf{p});\Delta\mathbf{q})^{-1} \tag{43}$$

In this expression $\mathbf{J_p}$ is an $m \times m$ matrix and $\mathbf{J_q}$ is an $4 \times 4$ matrix. The meaning of $\mathbf{J_p}$ is, for example, given a small change $\Delta\mathbf{p}$ to the warp parameters, how do the parameters of the right hand side of Equation (43) change. Both $\mathbf{J_p}$ and $\mathbf{J_q}$ depend on $\mathbf{p}$ and $\mathbf{q}$. We describe how to compute them (in combination with $\frac{\partial F_{t_i}}{\partial \mathbf{p}}$ and $\frac{\partial F_{t_i}}{\partial \mathbf{q}}$) in Appendix A. We experimentally verified that failure to take into account $\mathbf{J_p}$ and $\mathbf{J_q}$ in the inverse compositional update can cause the algorithm to fail, particularly for large pose variation. The 2D shape and the projection of the 3D shape diverge.

The Gauss-Newton inverse compositional algorithm to minimize Equation (41) then consists of iteratively computing:

$$\begin{pmatrix} \Delta\mathbf{p} \\ \Delta\mathbf{q} \\ \Delta\overline{\mathbf{p}} \\ \Delta\mathbf{P} \\ \Delta o_u \\ \Delta o_v \end{pmatrix} = -H_{3\mathrm{D}}^{-1} \left( \begin{pmatrix} \Delta\mathbf{p}_{\mathrm{SD}} \\ \Delta\mathbf{q}_{\mathrm{SD}} \\ \mathbf{0} \\ \mathbf{0} \\ 0 \\ 0 \end{pmatrix} + K \cdot \sum_{t=u,v} \sum_{i=1}^{n} \left[ \mathbf{SD}_{F_{t_i}} \right]^{\mathrm{T}} F_{t_i}(\mathbf{p}; \mathbf{q}; \overline{\mathbf{p}}; \mathbf{P}; o_u; o_v) \right) \tag{44}$$

where:

$$\mathbf{SD}_{F_{t_i}} = \left( \frac{\partial F_{t_i}}{\partial \mathbf{p}} \mathbf{J_p} \; \frac{\partial F_{t_i}}{\partial \mathbf{q}} \mathbf{J_q} \; \frac{\partial F_{t_i}}{\partial \overline{\mathbf{p}}} \; \frac{\partial F_{t_i}}{\partial \mathbf{P}} \; \frac{\partial F_{t_i}}{\partial o_u} \; \frac{\partial F_{t_i}}{\partial o_v} \right) \tag{45}$$

and:

$$H_{3\mathrm{D}} = \begin{pmatrix} H_{2\mathrm{D}} & \mathbf{0} & \mathbf{0} & 0 & 0 \\ \mathbf{0} & \mathbf{0} & \mathbf{0} & 0 & 0 \\ \mathbf{0} & \mathbf{0} & \mathbf{0} & 0 & 0 \\ 0 & 0 & 0 & 0 & 0 \\ 0 & 0 & 0 & 0 & 0 \end{pmatrix} + K \cdot \sum_{t=u,v} \sum_{i=1}^{n} \left[ \mathbf{SD}_{F_{t_i}} \right]^{\mathrm{T}} \left[ \mathbf{SD}_{F_{t_i}} \right]. \tag{46}$$

After the parameter updates have been computed using Equation (44), the warp is updated using Equation (32), the 3D shape parameters are updated $\overline{\mathbf{p}} \leftarrow \overline{\mathbf{p}} + \Delta\overline{\mathbf{p}}$, and the origin offsets are updated $o_u \leftarrow o_u + \Delta o_u$ and $o_v \leftarrow o_v + \Delta o_v$. The update to the camera matrix $\mathbf{P}$ is slightly more involved because there are only really 4 degrees of freedom. See Appendix A for the details.

Although Equations (44–46) may appear fairly complex, the problem is now $m + 4 + \overline{m} + 6$ dimensional rather than $m+4$ dimensional, and the only things that can be precomputed are the 2D steepest descent images $\mathbf{SD}_{2\mathrm{D}}(\mathbf{u})$ and the 2D Hessian $H_{2\mathrm{D}}$, implementing these equations does not take significantly more computation than implementing Equations (33) and (34). The reasons are: (1) the summations in Equations (44) and (46) are over $2n$ vertex $u$ and $v$ coordinates rather than over the thousands of pixels in the model $\mathbf{u} \in \mathbf{s}_0$, (2) as shown in Section 3, usually $\overline{m} \ll m$ and so the difference in dimensionality is not so great, and (3) this optimization is more constrained and so requires less iterations to converge (see experimental results below for more details.)

## 5.4 Qualitative Evaluation

In Figure 6 we include 4 examples of the 3D algorithm fitting to a single input image, 2 for Dataset 1 Figure 2), and 2 for Dataset 2 (Figure 3.) In the left column we display the initial configuration, in the middle column the results after 5 iterations, and in the right column the results after the algorithm has converged. In each case, we display the input image with the current estimate of the 3D shape mesh overlayed in white. The 3D shape is projected onto the image with the current camera matrix. In the top right of each image, we also include renderings of the 3D shape from two different viewpoints. In the top left of the image, we display estimates of the 3D pose extracted from the current estimate of the camera matrix $\mathbf{P}$. We also display the current estimate of the 2D shape as blue dots.

In Figure 7 we include 12 frames of the 3D algorithm being used to track faces. The results for Dataset 1 in the top 2 rows are examples tracking a subset of the 5 people used to build the model in Figure 2. The results for Dataset 2 in the bottom 2 rows are examples tracking people who were not in the training data used to build the model in Figure 3.

The range of convergence of the 3D fitting algorithm is sufficient to allow initialization and re-initialization from a face detector. We run the 3D tracking algorithm in a foreground thread. In a background thread we first run a real-time face detector and then apply the 3D tracking algorithm to the result. The foreground tracking thread is re-initialized whenever the background thread gives

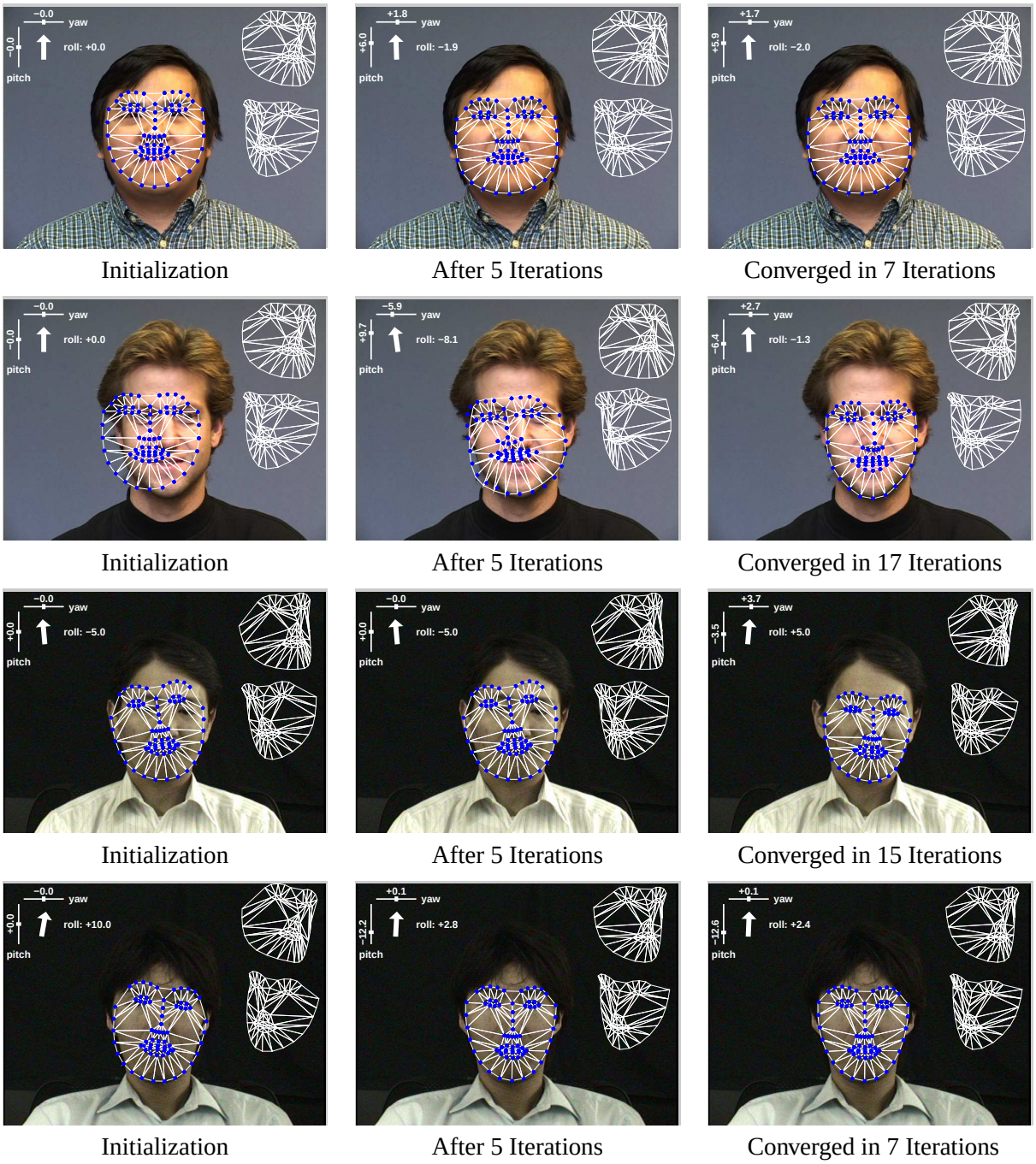


**Figure 6:** Examples of the 3D algorithm fitting to a single image, 2 for Dataset 1 in Figure 2, and 2 for Dataset 2 in Figure 3. We display the 3D shape estimate (white) projected onto the original image and also from a couple of other viewpoints in the top right of each image. In the top left of each image we display estimates of the 3D pose extracted from the current estimate of the camera matrix $\mathbf{P}$. We also display the 2D shape estimate (blue dots.)

a better fit than the foreground thread gave on the same frame. A few frames captured from the system are included in Figure 8. Overall, the tracking thread runs at 30Hz on a dual 3.0GHz PC,

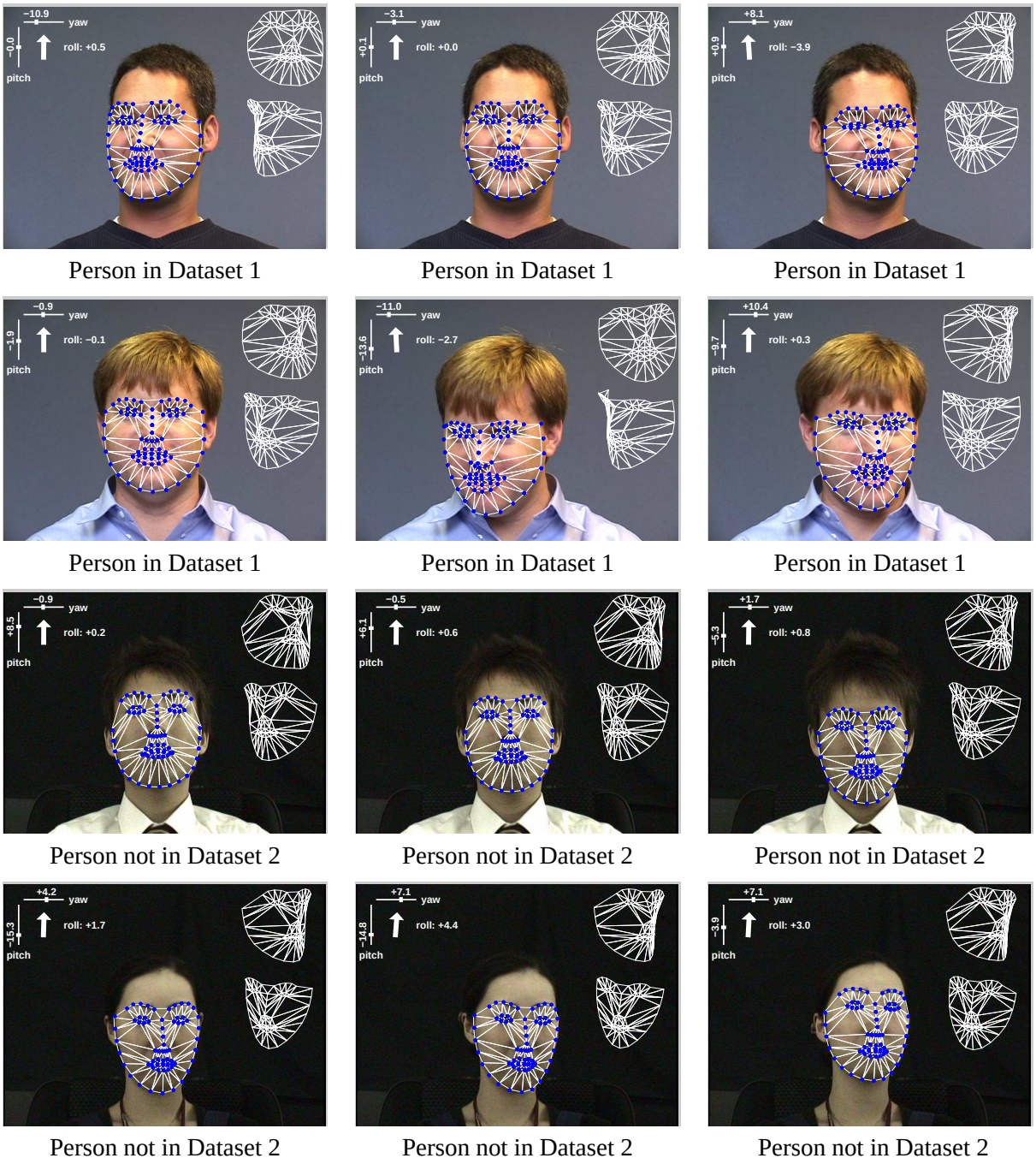


**Figure 7:** Example tracking results for the 5 people in Dataset 1 and 6 people not used to build the model in Dataset 2.

limited by the camera. See Section 5.6 for more details of the computational cost of the fitting algorithm.

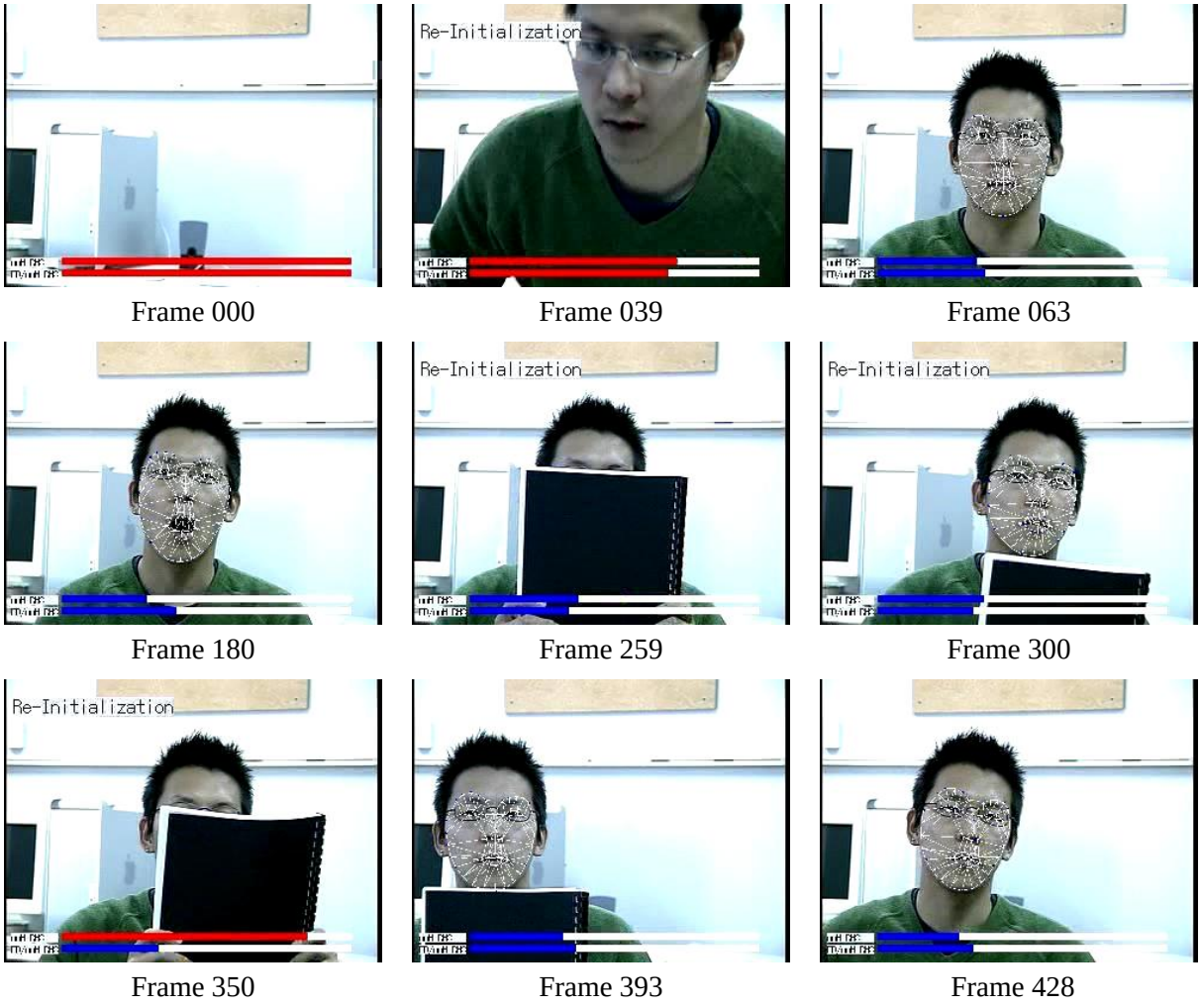


**Figure 8:** A few frames illustrating our integrated real-time 3D tracking system, with automatic initialization and re-initialization using a face detector. The subject enters the field of view of the camera. The face detector finds their face and initializes the tracker. When the person occludes their face temporally, the tracker is re-initialized after the face becomes visible again. Overall, the tracking thread in the system runs at 30Hz on a dual 3.0GHz PC, limited by the camera.

## 5.5 Quantitative Comparison: 2D Fitting vs. 3D Fitting

Directly comparing the fitting performance of 2D AAMs [Cootes *et al.*, 2001] and 3DMMs [Blanz and Vetter, 1999] is difficult because of the numerous small differences in the models and algorithms. See Section 2.3. On the other hand, comparing the 2D fitting algorithm [Matthews and Baker, 2004] with the 3D fitting algorithm is a more direct comparison of the inherent properties of 2D and 3D face models. Almost all of the code in the two algorithms is the same. The 3D algorithm just has a little extra code to deal with the second term in Equation (39).

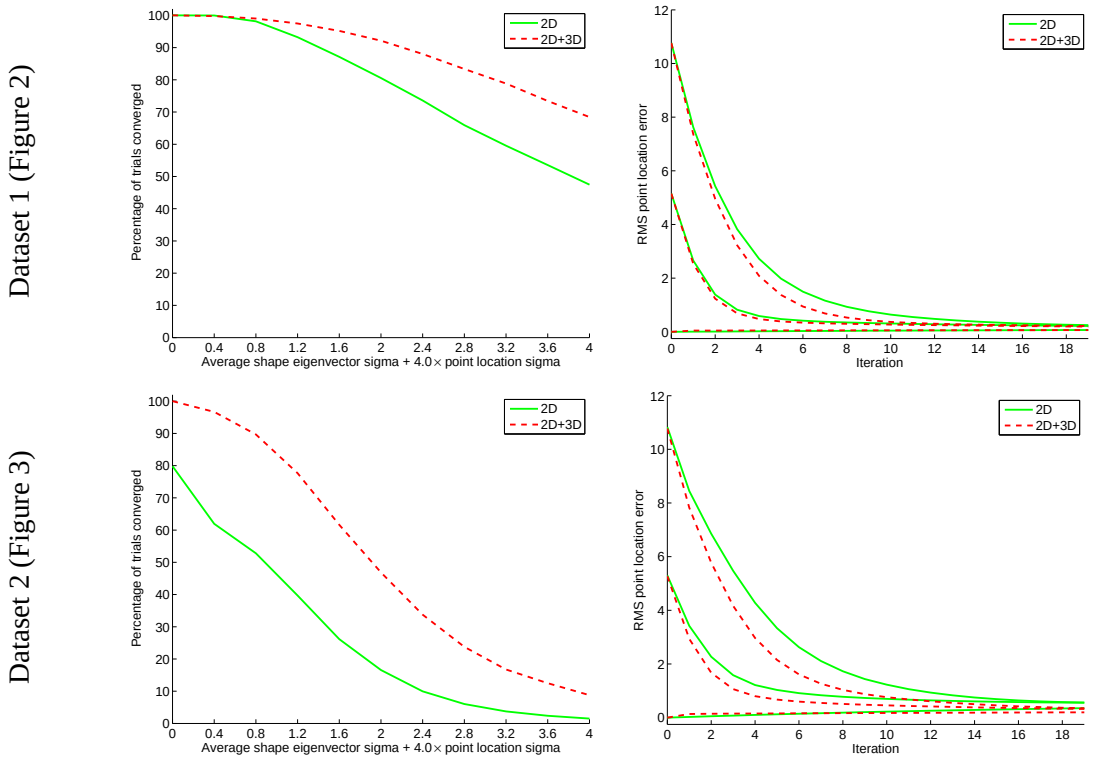


(A) Fitting Robustness (B) Rate of Convergence

**Figure 9:** A comparison of the fitting robustness and rate of convergence of the 2D fitting algorithm [Matthews and Baker, 2004] with the 3D fitting algorithm following the same evaluation protocol as [Matthews and Baker, 2004]. The results show that the 3D algorithm is both more robust (A) than the 2D algorithm and converges faster (B) in terms of number of iterations.

In Figure 9 we present results comparing the fitting robustness and rate of convergence of the 2D fitting algorithm [Matthews and Baker, 2004] with the 3D fitting algorithm, following the protocol in [Matthews and Baker, 2004]. In the top row we present results for Dataset 1 (Figure 2) and in the bottom row for Dataset 2 (Figure 3.) In the left column we present fitting robustness results. These results are generated by first generating ground-truth for each algorithm by tracking a set of videos. For Dataset 1 we use 828 frames from 5 videos of the 5 subjects in the training set. For Dataset 2 we use 900 frames from 6 videos of 6 subjects *not* in the training set. For each frame we then generate a number of trials by perturbing the 2D shape parameters from the ground-truth. We follow the procedure in [Matthews and Baker, 2004] and weight the similarity and 2D shape parameters so that the algorithms would be approximately equally likely to convergence if perturbed independently in similarity and shape. We generate 20 trials for each of a set of larger

and larger perturbations. We then run both fitting algorithms from the perturbed ground-truth and determine whether they converge by comparing the final RMS 2D shape error with the ground-truth. In particular, we used a threshold of 1.0 pixels to define convergence.

The rate of convergence results in the right column are generated by perturbing away from the ground-truth in a similar manner. In this case we consider 2 different perturbation magnitudes, which result in the 2 curves for each algorithm. For each set of trials, we compute the average RMS pixel error after each iteration for all of the trials that end up converging to within 1.0 pixels. We then plot this value against the iteration number, resulting in the plots in Figure 9(B).

The results in Figure 9 show that the 3D fitting algorithm is both more robust than the 2D algorithm [Matthews and Baker, 2004] (A) and converges faster (B) in terms of the number of iterations. The results hold for both datasets. The improvement in performance is slightly more for the harder Dataset 2 (where the fitting is to subjects not in the training data) than for Dataset 1 (where the fitting it to subjects in the training data). The fact that the 3D algorithm is more robust than the 2D algorithm may at first glance be surprising; the 3D optimization is higher dimensional and so it might be expected to suffer from more local minima. This reasoning is incorrect. Because the 2D model can generate "physically unrealizable" model instances (see Section 3.2), it is actually more prone to local minima than a 2D model constrained to only move as though it were 3D.

## 5.6 Computational Cost

In Table 1 we compare the fitting speed of the 3D fitting algorithm with that of the 2D fitting algorithm [Matthews and Baker, 2004]. We include results for both the model in Dataset 1 (8 2D shape modes, 4 similarity parameters, 40 appearance modes, 4 3D shape modes, 6 camera parameters, and 29,976 color pixels) and the model in Dataset 2 (9 2D shape modes, 4 similarity parameters, 59 appearance modes, 4 3D shape modes, 6 camera parameters, and 30,000 color pixels). The 2D fitting algorithm [Matthews and Baker, 2004] operates at 70–80 frames per second and the 3D fitting algorithm operates at 65–70 frames per second, both results computed on a dual, dual-core 2.5GHz PowerPC Macintosh G5 with 4GB of RAM. Note that the 3D algorithm requires

**Table 1:** Fitting speed comparison on a dual, dual-core 2.5GHz PowerPC Macintosh G5 with 4GB of RAM. We include results for both the model in Dataset 1 (8 2D shape modes, 4 similarity parameters, 40 appearance modes, 4 3D shape modes, 6 camera parameters, and 29,976 color pixels) and the model in Dataset 2 (9 2D shape modes, 4 similarity parameters, 59 appearance modes, 4 3D shape modes, 6 camera parameters, and 30,000 color pixels). Although the 3D algorithm is slightly slower than the 2D algorithm, it still operates comfortably in real-time, and requires slightly fewer iterations to converge.

| | 2D Fitting | | 3D Fitting | |
|---|---|---|---|---|
| | Frames per Second | Iterations per Frame | Frames per Second | Iterations per Frame |
| Dataset 1 | 73.1 | 2.74 | 65.4 | 2.72 |
| Dataset 2 | 80.9 | 2.65 | 71.2 | 2.26 |

slightly fewer iterations to converge on average than the 2D algorithm, particularly for Dataset 2, further validating the results in Figure 9(B).

## 5.7 Summary

Although fitting 2D face models in real-time is possible using the inverse compositional algorithm, we have outlined in Section 5.2 why naively extending this algorithm to 3D is not possible. We also presented a solution to this difficulty, the simultaneous fitting of both a 2D and a 3D model. The result is a real-time 3D model fitting algorithm. Experimental results show 3D model fitting to be both inherently more robust and converge in fewer iterations than 2D model fitting, confirming that 3D is a more natural parameterization of faces than 2D.

Another possible approach to 3D model fitting is the one taken in [Romdhani and Vetter, 2003]. Due to the density of their models and a variety of other details, the current implementation of their algorithm is quite slow, requiring several seconds per frame. There seems to be no theoretical reason why the algorithm could not be implemented in real-time for the models of the complexity used in this paper. Romdhani and Vetter avoid the difficulty in 3D fitting described in Section 5.2 by "un-rolling" the 2D surface in 3D space and posing the problem as mapping from a 2D texture space to a 2D image. The 3D shape $\overline{\mathbf{p}}$ and the camera matrix $\mathbf{P}$ are embedded in a 2D shape warp $\mathbf{W}(\mathbf{u};\mathbf{p})$ rather than a 3D shape warp $\mathbf{W}(\mathbf{x};\overline{\mathbf{p}})$. The 2D inverse compositional algorithm is not directly applicable to the un-rolled texture maps because the identity warp is not one of the warps

$\mathbf{W}(\mathbf{u};\mathbf{p})$ [Baker and Matthews, 2004]. Romdhani and Vetter avoid this problem by generalizing the inverse compositional algorithm to allow a warp update:

$$\mathbf{W}(\mathbf{u};\mathbf{p}) \leftarrow \mathbf{W}(\mathbf{u};\mathbf{p}) \circ \mathbf{W}(\mathbf{u};\mathbf{p}^\dagger)^{-1} \circ \mathbf{W}(\mathbf{u};\mathbf{p}^\dagger + \Delta\mathbf{p}) \tag{47}$$

where $\mathbf{p}^\dagger$ is a fixed vector of parameters. This equation should be compared with the usual update in Equation (32). The incremental warp is $\mathbf{W}(\mathbf{u};\mathbf{p}^\dagger) \circ \mathbf{W}(\mathbf{u};\mathbf{p}^\dagger + \Delta\mathbf{p})^{-1}$ rather than $\mathbf{W}(\mathbf{u};\Delta\mathbf{p})$. This definition of the update leads to the Jacobians of the warp being evaluated at $\mathbf{p}^\dagger$ leading to a dependence on $\mathbf{p}^\dagger$. Empirically, the authors find that the algorithm performs better when $\mathbf{p} \approx \mathbf{p}^\dagger$. To ameliorate this undesirable property, the authors pre-compute the steepest descent images and Hessian for multiple different $\mathbf{p}^\dagger$ and use the closest one in the online phase of the algorithm. A direct comparison between our 3D fitting algorithm and the algorithm in [Romdhani and Vetter, 2003] on the same 3D model is outside the scope of this paper which focuses on comparing 2D and 3D face models. However, such a comparison is an interesting area for future work.

# 6 Self Occlusion Reasoning

In Section 6.1 we briefly describe how to implement a "z-buffer" for a 3D model [Foley *et al.*, 1990]. In Section 6.2 we describe an approximation to this algorithm for 2D models. In Section 6.3 we empirically compare the performance of the 2 algorithms.

## 6.1 Software Z-Buffering for 3D Models

Perhaps the easiest way to detect self occlusion with a 3D model is to implement a "z-buffer" [Foley *et al.*, 1990]. The first step is to compute the depth of every 3D mesh vertex. The "z" axis of the camera $\mathbf{P}$ in Equation (7) is $(k_x, k_y, k_z) = (i_x, i_y, i_z) \times (j_x, j_y, j_z)$ where $\times$ is the vector

cross product. The depths of the mesh vertices are then given by:

$$(k_x\, k_y\, k_z)\, \bar{\mathbf{s}} \;=\; (k_x\, k_y\, k_z) \begin{pmatrix} x_1 & x_2 & \dots & x_{\overline{n}} \\ y_1 & y_2 & \dots & y_{\overline{n}} \\ z_1 & z_2 & \dots & z_{\overline{n}} \end{pmatrix}. \tag{48}$$

A z-buffer is then set up consisting of an image the size of the input image $I$, with all depth values initialized as invalid. We compute the z-buffer by raster scanning each triangle in the face model projected into $I$. For each pixel, we compute the depth of that pixel as a linear combination of the depths of the triangle vertices (using the same mixing parameters $\alpha$ and $\beta$ used in [Matthews and Baker, 2004].) If the depth value in the z-buffer at this pixel is either still invalid or is greater than the depth just computed for this pixel, we update the depth. If the depth value in the z-buffer is less than the depth just computed for this pixel, the z-buffer is not updated.

The z-buffer is then used to determine self-occlusion in the following manner. We raster scan the base mesh $\mathbf{s}_0$ in the usual manner while we are computing $I(\mathbf{N}(\mathbf{W}(\mathbf{u};\mathbf{p});\mathbf{q}))$. We look up the triangle identity of each pixel and compute the destination of the pixel under the warp. We then index into the z-buffer at this location (using bilinear interpolation), and also compute the depth of this point in the same way we computed the z-buffer. If the depth matches that in the z-buffer (within a small threshold) the pixel is visible. If the depths do not match this pixel is occluded.

If the face model completely wraps around the entire head and forms a closed surface with no boundary, this z-buffering algorithm is sufficient to determine occlusion. If the model does have a boundary it is also necessary to check for flipped triangles using the algorithm described below. All of the pixels from a flipped triangle are occluded and should be ignored.

## 6.2 Approximate Self-Occlusion for 2D Models

Self occlusion reasoning for 2D models is harder than for 3D models. However, for objects such as faces that are approximately convex, it is often sufficient to just check which triangles in the 2D mesh are facing towards the camera. All triangles that are not facing towards the camera must be

self occluded. This algorithm is an approximation to the 3D z-buffering algorithm for non-convex objects. Only for a convex object are all forwards facing triangles visible, and vice versa.

On the other hand, this 2D algorithm: (1) is easy to implement and is very efficient, (2) computes a measure of how frontal the triangle is that can be used as a confidence value to weight the triangles, and (3) can always be combined with a robust fitting algorithm such as [Gross *et al.*, 2004] to cope with the residual self-occlusions and occlusions by other objects

Whether a triangle is forwards facing or not can be determined as follows. Suppose that the 2D coordinates of the three vertices of the triangle in the mean shape are $(u_i^0, v_i^0)^{\mathrm{T}}$, $(u_j^0, v_j^0)^{\mathrm{T}}$, and $(u_k^0, v_k^0)^{\mathrm{T}}$. Also suppose that the 2D coordinates of the three vertices of the corresponding triangle in the input image are $(u_i, v_i)^{\mathrm{T}}$, $(u_j, v_j)^{\mathrm{T}}$, and $(u_k, v_k)^{\mathrm{T}}$. We then compute:

$$F = \frac{\begin{pmatrix} u_j - u_i \\ v_j - v_i \end{pmatrix} \cdot \begin{pmatrix} -(v_k - v_i) \\ u_k - u_i \end{pmatrix}}{\begin{pmatrix} u_j^0 - u_i^0 \\ v_j^0 - v_i^0 \end{pmatrix} \cdot \begin{pmatrix} -(v_k^0 - v_i^0) \\ u_k^0 - u_i^0 \end{pmatrix}}. \tag{49}$$

If $F > 0$ the triangle is forwards facing. If $F < 0$ the triangle is backwards facing. If $F = 0$ the triangle is degenerate; i.e. the projection of the triangle into the input image is a line. As mentioned above, the indicator function $F$ can also be used as a measure of how frontal the triangle is. The larger (the relative value of) $F$ is, the more frontal the triangle is, the smaller the more oblique.

## 6.3 Experimental Results

Since faces are very close to convex, empirically the 2D "flipped triangle" algorithm is a reasonable approximation to the 3D z-buffering algorithm. In Figure 10 we show 3 examples of occlusion masks computed for a face model at a variety of poses. For a yaw angle of 30 degrees the nose and the cheek self-occlude some of the face. The 2D flipped triangle algorithm gives a reasonable, but not perfect estimate of the occlusion. For a yaw angle of 60 degrees almost the entire right half of the face is occluded. Again, the 2D flipped triangles algorithm gives a reasonable estimate.

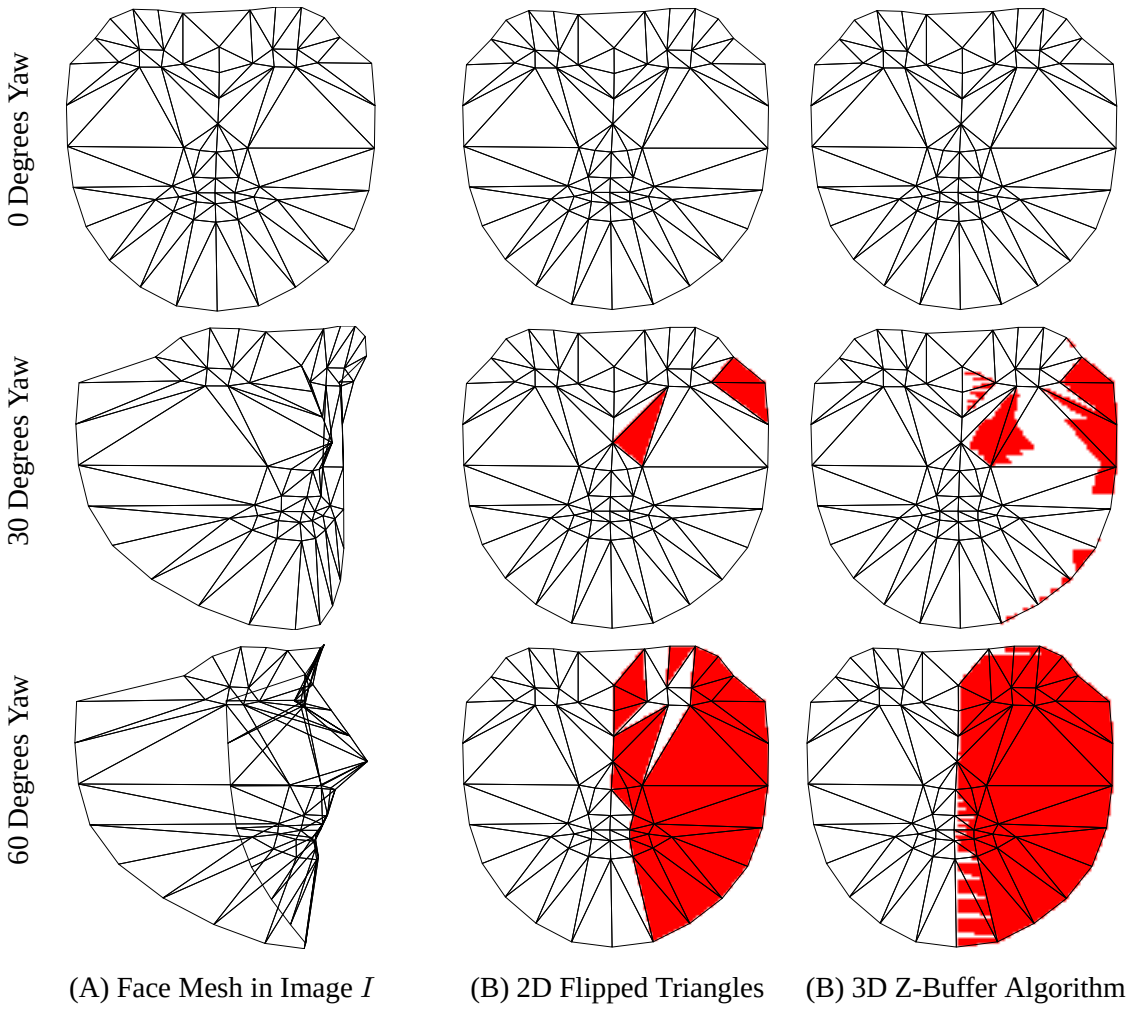


**Figure 10:** A few example occlusion masks. (A) The input face mesh in the input image $I$. (B) The results computed using only the 2D information in the "flipped-triangles". (C) The results of also using the 3D face model and a z-buffering algorithm. Because faces are close to convex, the results for the 2D and 3D algorithms are reasonably similar. See Figure 11 for a quantitative comparison.

In Figure 11 we include quantitative results, independently varying the yaw and pitch of the face. For each head pose, we generated 100 random samples of the 3D face shape using the likelihoods implied in the Gaussian interpretation of PCA. For each sample, we compute the percentage of pixels misclassified by the 2D algorithm. In Figure 11 we plot this measure independently across yaw and pitch variation of the head. We plot both the results obtained for the mean 3D shape, and error bars representing 2 standard deviations of the results obtained by randomly sampling the non-rigid shape variation. The results show that in all cases, less than 10% of pixels are missclassified by the 2D "flipped-triangles" algorithm; i.e. the 2D algorithm gives a reasonable

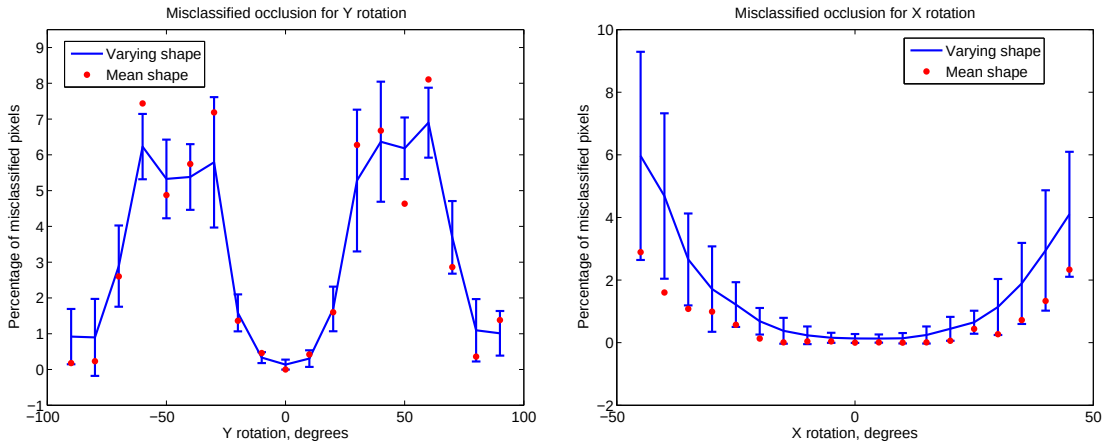


(A) Varying Yaw (B) Varying Pitch

**Figure 11:** A quantitative comparison of the 2D and 3D occlusion reasoning algorithms. We independently sampled the yaw and pitch components of the head pose. For each head pose, we generated 100 random samples of the 3D face shape and computed the average percentage of pixels misclassified by the 2D algorithm. We plot both the results obtained for the mean 3D shape, and error bars representing 2 standard deviations of the results obtained by randomly sampling the non-rigid shape variation. In all cases, less than 10% of pixels are misclassified. The peaks in both curves are caused by the nose self-occluding the rest of the face.

approximation to the 3D algorithm. The two peaks in Figure 11(A) and the peaks at the extreme poses in Figure 11(B) are both caused by the nose self occluding the face.

### 6.4 Summary

Although self occlusion reasoning is conceptually easier for 3D models than for 2D, simply determining which triangles are flipped gives a reasonable 2D approximation to the 3D z-buffering algorithm. The real value of the binary indicator function that determines whether a triangle is flipped or not is also a good measure of how reliable the pixels in each triangle are.

## 7 Conclusion

We have compared 2D and 3D face models along a variety of axes. The main conclusion is that 3D models are overall preferable to 2D models. The 3D parameterization is more compact (up to 6 times fewer parameters), more natural (i.e. head pose and non-rigid shape deformation are

separated), 3D model fitting is more robust and requires fewer iterations to converge, and 3D occlusion reasoning is more powerful. Two of the frequently cited negatives of 3D models, slow fitting and construction requiring range data, have been addressed. We have presented a linear non-rigid structure-from-motion algorithm [Xiao *et al.*, 2004b] for the construction of a 3D model from 2D tracking results and a real-time 3D model fitting algorithm [Xiao *et al.*, 2004a]. One final benefit of 3D models is that multi-camera model fitting is far easier [Koterba *et al.*, 2005].

On the other hand, the differences between 2D and 3D models are not as great as is sometimes claimed. Ignoring the size of the model and assuming a scaled orthographic camera, 2D models have the same representational power as 3D, separating the head pose from the non-rigid head shape deformation is possible, and approximate occlusion reasoning is possible. The one limitation of 2D models that is hard to avoid is that fitting them is inherently less robust than 3D. The underlying cause of this problem is the "over-parameterization" of 2D models and the resulting ability to generate numerous "physically unrealizable" model instances. See Section 3.2.

# Acknowledgments

The research described in this paper was supported in part by Denso Corporation, U.S. Department of Defense contract N41756-03-C4024, and National Institute of Mental Health grant R01 MH51435. A preliminary version appeared in the 2004 IEEE Conference on Computer Vision and Pattern Recognition [Xiao *et al.*, 2004a]. We thank the reviewers of that paper for their feedback. We also thank Tim Cootes, Sami Romdhani, and Thomas Vetter for their comments. We also thank our collaborators at CMU for their input, including Ralph Gross, Seth Koterba, Jeff Cohn, Changbo Hu, Raju Patil, Goksel Dedeoglu, Krishnan Ramnath, Takahiro Ishikawa, German Cheung, Adrian Broadhurst, Junya Inada, and last but not least, Takeo Kanade.

# References


[Baker and Matthews, 2001] S. Baker and I. Matthews. Equivalence and efficiency of image alignment algorithms. In *Proceedings of the IEEE Conference on Computer Vision and Pattern Recognition*, volume 1, pages 1090–1097, 2001.

[Baker and Matthews, 2004] S. Baker and I. Matthews. Lucas-Kanade 20 years on: A unifying framework. *International Journal of Computer Vision*, 56(3):221 – 255, 2004.

[Baker *et al.*, 2003] S. Baker, R. Gross, and I. Matthews. Lucas-Kanade 20 years on: A unifying framework: Part 3. Technical Report CMU-RI-TR-03-35, Carnegie Mellon University Robotics Institute, 2003.

[Baker *et al.*, 2004a] S. Baker, R. Gross, and I. Matthews. Lucas-Kanade 20 years on: Part 4. Technical Report CMU-RI-TR-04-14, Carnegie Mellon University Robotics Institute, 2004.

[Baker *et al.*, 2004b] S. Baker, R. Patil, K.M. Cheung, and I. Matthews. Lucas-Kanade 20 years on: Part 5. Technical Report CMU-RI-TR-04-64, Carnegie Mellon University Robotics Institute, 2004.

[Blanz and Vetter, 1999] V. Blanz and T. Vetter. A morphable model for the synthesis of 3D faces. In *Computer Graphics, Annual Conference Series (SIGGRAPH)*, pages 187–194, 1999.

[Brand, 2001] M. Brand. Morphable 3D models from video. In *Proceedings of the IEEE Conference on Computer Vision and Pattern Recognition*, volume 2, pages 456–463, 2001.

[Cootes *et al.*, 2001] T. Cootes, G. Edwards, and C. Taylor. Active appearance models. *IEEE Transactions on Pattern Analysis and Machine Intelligence*, 23(6):681–685, 2001.

[Foley *et al.*, 1990] J. Foley, A. van Dam, S. Feiner, and J. Hughes. *Computer Graphics: Principles and Practice*. Addison-Wesley, second edition, 1990.

[Gross *et al.*, 2004] R. Gross, I. Matthews, and S. Baker. Constructing and fitting active appearance models with occlusion. In *Proceedings of the IEEE Workshop on Face Processing in Video*, pages 72–79, 2004.

[Hager and Belhumeur, 1998] G. Hager and P. Belhumeur. Efficient region tracking with parametric models of geometry and illumination. *IEEE Transactions on Pattern Analysis and Machine Intelligence*, 20(10):1025–1039, 1998.

[Ishikawa *et al.*, 2004] T. Ishikawa, S. Baker, I. Matthews, and T. Kanade. Passive driver gaze tracking with active appearance models. In *Proceedings of the 11th World Congress on Intelligent Transportation Systems*, 2004. URL: http://www.ri.cmu.edu/pubs/pub_4705.html.

[Kanade, 1973] T. Kanade. *Picture Processing System by Computer Complex and Recognition of Human Faces*. PhD thesis, Kyoto University, November 1973.

[Koterba *et al.*, 2005] S. Koterba, S. Baker, I. Matthews, C. Hu, J. Xiao, J. Cohn, and T. Kanade. Multi-view aam fitting and camera calibration. In *Proceedings of the IEEE International Conference on Computer Vision*, pages 511–518, 2005.

[Lanitis *et al.*, 1997] A. Lanitis, C. Taylor, and T. Cootes. Automatic interpretation and coding of face images using flexible models. *IEEE Transactions on Pattern Analysis and Machine Intelligence*, 19(7):742–756, 1997.

[Lucas and Kanade, 1981] B. Lucas and T. Kanade. An iterative image registration technique with an application to stereo vision. In *Proceedings of the International Joint Conference on Artificial Intelligence*, pages 674–679, 1981.

[Matthews and Baker, 2004] I. Matthews and S. Baker. Active Appearance Models revisited. *International Journal of Computer Vision*, 60(2):135–164, 2004.

[Matthews *et al.*, 2002] I. Matthews, T. Cootes, A. Bangham, S. Cox, and R. Harvery. Extraction of visual features for lipreading. *IEEE Transactions on Pattern Analysis and Machine Intelligence*, 24(2):198–213, 2002.

[Romdhani and Vetter, 2003] S. Romdhani and T. Vetter. Efficient, robust and accurate fitting of a 3D morphable model. In *Proceedings of the International Conference on Computer Vision*, volume 1, pages 59–55, 2003.

[Rowley *et al.*, 1998] H.A. Rowley, S. Baluja, and T. Kanade. Neural network-based face detection. *IEEE Transactions on Pattern Analysis and Machine Intelligence*, 20(1):23–38, 1998.

[Shum and Szeliski, 2000] H.-Y. Shum and R. Szeliski. Construction of panoramic image mosaics with global and local alignment. *International Journal of Computer Vision*, 16(1):63–84, 2000.

[Tian *et al.*, 2001] Y. Tian, T. Kanade, and J. Cohn. Recognizing action units for facial expression analysis. *IEEE Transactions on Pattern Analysis and Machine Intelligence*, 23(2):97–115, 2001.

[Tomasi and Kanade, 1992] C. Tomasi and T. Kanade. Shape and motion from image streams under orthography: A factorization method. *International Journal of Computer Vision*, 9(2):137–154, 1992.

[Torresani *et al.*, 2001] L. Torresani, D. Yang, G. Alexander, and C. Bregler. Tracking and modeling non-rigid objects with rank constraints. In *Proceedings of the IEEE Conference on Computer Vision and Pattern Recognition*, volume 1, pages 493–500, 2001.

[Xiao *et al.*, 2004a] J. Xiao, S. Baker, I. Matthews, and T. Kanade. Real-time combined 2D+3D Active Appearance Models. In *Proceedings of the IEEE Conference on Computer Vision and Pattern Recognition*, volume 2, pages 535–542, 2004.

[Xiao *et al.*, 2004b] J. Xiao, J. Chai, and T. Kanade. A closed-form solution to non-rigid shape and motion recovery. In *Proceedings of the European Conference on Computer Vision*, volume 4, pages 573–587, 2004.

# A Computing the Steepest Descent Geometry $\mathbf{SD}_{F_{t_i}}$

In Section 5.3 we omitted the details of how the steepest descent geometry constraints:

$$\mathbf{SD}_{F_{t_i}} = \left( \frac{\partial F_{t_i}}{\partial \mathbf{p}} \mathbf{J}_\mathbf{p} \frac{\partial F_{t_i}}{\partial \mathbf{q}} \mathbf{J}_\mathbf{q} \frac{\partial F_{t_i}}{\partial \overline{\mathbf{p}}} \frac{\partial F_{t_i}}{\partial \mathbf{P}} \frac{\partial F_{t_i}}{\partial o_u} \frac{\partial F_{t_i}}{\partial o_v} \right) \tag{50}$$

are computed. The first two components of $\mathbf{SD}_{F_{t_i}}$ are computed as follows. Since the only component of $F_{t_i}$ that includes $\mathbf{p}$ or $\mathbf{q}$ is $\mathbf{N}\left(\mathbf{s}_0 + \sum_{i=1}^{m} p_i \, \mathbf{s}_i; \mathbf{q}\right)$, $\frac{\partial F_{t_i}}{\partial \mathbf{p}} \mathbf{J}_\mathbf{p}$ is the (negative of the) rate of change of the destination of the warp in the right hand side of Equation (42) with respect to $\Delta\mathbf{p}$. Similarly, $\frac{\partial F_{t_i}}{\partial \mathbf{q}} \mathbf{J}_\mathbf{q}$ is the (negative of the) rate of change of the destination of the warp in the right hand side of Equation (42) with respect to $\Delta\mathbf{q}$. These two expressions can be estimated by setting each of the parameters in $\Delta\mathbf{p}$ and $\Delta\mathbf{q}$ in turn to be a small value (say, 1.0), setting all the other parameters to be 0.0, and then using the warp composition (see [Matthews and Baker, 2004]) to estimate the perturbation to the destination of the right-hand side of Equation (42).

The other components of $\mathbf{SD}_{F_{t_i}}$ are somewhat simpler:

$$\frac{\partial F_{t_i}}{\partial \overline{p}_j} = \mathbf{P}\mathbf{s}_j, \qquad \frac{\partial F_{t_i}}{\partial o_u} = \begin{pmatrix} 1 & \dots & 1 \\ 0 & \dots & 0 \end{pmatrix}, \qquad \frac{\partial F_{t_i}}{\partial o_v} = \begin{pmatrix} 0 & \dots & 0 \\ 1 & \dots & 1 \end{pmatrix}. \tag{51}$$

The camera matrix $\mathbf{P}$ is more complicated because it has 6 variables, but only 4 degrees of freedom. We perform the update similarly to how 3D rotations are treated in [Shum and Szeliski, 2000]. We first extract the scale from the matrix:

$$\mathbf{P} = \sigma \begin{pmatrix} i_x & i_y & i_z \\ j_x & j_y & j_z \end{pmatrix} \tag{52}$$

and constrain the projection axes $\mathbf{i} = (i_x, i_y, i_z)$ and $\mathbf{j} = (j_x, j_y, j_z)$ to be orthonormal. We compute

the update to the scale $\Delta\sigma$ using:

$$\frac{\partial F_{t_i}}{\partial \sigma} \;=\; \begin{pmatrix} i_x & i_y & i_z \\ j_x & j_y & j_z \end{pmatrix} \mathbf{s} \tag{53}$$

where $\mathbf{s} = \left(\bar{\mathbf{s}}_0 + \sum_{i=1}^{\overline{m}} \bar{p}_i \, \bar{\mathbf{s}}_i\right)$ and then update the scale $\sigma \leftarrow \sigma + \Delta\sigma$. We also compute small angle updates $\Delta\theta_x$, $\Delta\theta_y$, $\Delta\theta_z$ to the camera matrix using:

$$\frac{\partial F_{t_i}}{\partial \Delta\theta_x} \;=\; \mathbf{P} \begin{pmatrix} 0 & 0 & 0 \\ 0 & 0 & -1 \\ 0 & 1 & 0 \end{pmatrix} \mathbf{s}, \quad \frac{\partial F_{t_i}}{\partial \Delta\theta_y} \;=\; \mathbf{P} \begin{pmatrix} 0 & 0 & 1 \\ 0 & 0 & 0 \\ -1 & 0 & 0 \end{pmatrix} \mathbf{s}, \quad \frac{\partial F_{t_i}}{\partial \Delta\theta_y} \;=\; \mathbf{P} \begin{pmatrix} 0 & -1 & 0 \\ 1 & 0 & 0 \\ 0 & 0 & 0 \end{pmatrix} \mathbf{s} \tag{54}$$

update the camera matrix:

$$\mathbf{P} \;\leftarrow\; \mathbf{P} \begin{pmatrix} 1 & -\Delta\theta_z & \Delta\theta_y \\ \Delta\theta_z & 1 & -\Delta\theta_x \\ -\Delta\theta_y & \Delta\theta_x & 1 \end{pmatrix} \tag{55}$$

and finally reinforce the orthonormality constraints on $\mathbf{P}$.